# An improved channel model for medical body area network device testing

**Fenot Hailemichael**

**School of Electrical Engineering**

Thesis submitted for examination for the degree of Master of Science in Technology.
Espoo 08.12.2017

**Thesis supervisor:**

Prof. Katsuyuki Haneda

**Thesis advisor:**

M.Sc. (Tech.) Timo Toivanen

Aalto University
School of Electrical
Engineering

AALTO UNIVERSITY
SCHOOL OF ELECTRICAL ENGINEERING

ABSTRACT OF THE
MASTER'S THESIS

Author: Fenot Hailemichael

Title: An improved channel model for medical body area network device testing

Date: 08.12.2017 Language: English Number of pages: 11+71

Department of Radio Science and Technology
Professorship: Radio Science and Engineering

Supervisor: Prof. Katsuyuki Haneda
Advisor: M.Sc. (Tech.) Timo Toivanen

For testing and validation of medical body area network devices the knowledge of the wireless channel is very crucial. Although this could be implemented by utilizing existing BAN channel models, their restriction to specific device usage scenarios and environments make them less appropriate. For this purpose, this thesis presents a methodology for an MBAN device testing by developing an improved channel model which accounts for a room size and use case variability. The improved channel model is based on channel sounding, over the frequency band from 2.3 GHz to 2.5 GHz, performed for five different use cases defined based on body posture, movement, and orientation. In order to study the room size effect, the measurements have been carried out in three different office rooms and an anechoic chamber. The proposed channel model is composed of three components which are modeled separately: the mean path loss, body shadowing, and multipath fading. The mean path loss is modeled as a distance log function, while the body shadowing is modeled statistically by a lognormal distribution, and the multipath fading by a Rician distribution. The impact of room size is mainly notified in the Rician K-factor value; whereas the effect of movement is notified in the lognormal parameter. Furthermore, the effect of body orientation and posture is represented in the path loss model parameters.

Keywords: MBAN, channel modeling, Rician fading, Lognormal shadowing, channel sounding, indoor propagation

# Preface

This thesis work has been carried out in GE Healthcare Finland OY. I want to thank Engineering Manager Timo Toivanen, and the company in general, for giving me the opportunity to work in this interesting topic. Moreover, I would like to extend my gratitude to my supervisor, Associate Professor Katsuyuki Haneda, for his continuous guidance and support throughout the work. In addition, I want to thank Miah Md Suzan for his valuable comments during our meetings. Likewise, I would like to thank Anya Siddiqi for her guidance on academic writing.

Big thanks to Teodor Blaga not only for volunteering to perform the measurements, but also for his everyday support in various aspects. Thanks also to Timo Hakala for always being there to share his knowledge on wireless communication.

Finally, I want to thank my Family and friends for their love and support throughout these years.

Otaniemi, 26.11.2017

Fenot D. Hailemichael

# Contents

# Symbols and abbreviations

## Symbols

| | |
|---|---|
| $A$ | amplitude of dominant component |
| $A_{\mathrm{Rx}}$ | aperture area of receiver antenna |
| $B_{\mathrm{coh}}$ | coherence bandwidth |
| $c$ | speed of light |
| $d$ | antenna separation distance |
| $\mathcal{F}^{-1}$ | inverse Fourier transform |
| $f$ | frequency |
| $G_{\mathrm{Tx}}$ | gain of transmitter antenna |
| $G_{\mathrm{Rx}}$ | gain of receiver antenna |
| $H$ | transfer function of a channel |
| $I_0$ | modified Bessel function |
| $J_0$ | Bessel function |
| j | imaginary unit |
| $K_r$ | Rice factor |
| $L_P$ | mean path loss |
| $n$ | path loss exponent |
| $P$ | power |
| $p$ | polarization efficiency |
| $q$ | matching efficiency |
| $S_{11}$ | reflection coefficient |
| $S_{21}$ | transmission coefficient |
| $t_{\mathrm{coh}}$ | coherence time |
| | |
| $\epsilon$ | dielectric constant |
| $\theta$ | polar angle |
| $\lambda$ | wavelength |
| $\mu$ | mean |
| $\boldsymbol{\rho}_f$ | frequency correlation matrix |
| $\boldsymbol{\rho}_t$ | time correlation matrix |
| $\sigma$ | standard deviation |
| $\sigma_\tau$ | RMS delay |
| $\tau$ | delay |
| $\tau_0$ | delay of the LOS component |
| $\tau_k$ | delay of the k-th multipath component |
| $\overline{\tau}$ | mean excess delay |

## Abbreviations

| | |
|---|---|
| BAN | Body Area Network |
| CDF | Cumulative Distribution Function |
| EC | European Commission |
| EM | Electromagnetic |
| FCC | Federal Communications and Commission |
| FDTD | Finite Difference Time Domain |
| ISI | Inter Symbol Interference |
| ISM | Industrial Scientific Medical |
| LOS | Line-of-Sight |
| MBAN | Medical Body Area Network |
| MOM | Method of Moments |
| MPC | Multipath components |
| NLOS | None-Line-of-Sight |
| PDF | Probability Density Function |
| QLOS | Quasi-Line-of-Sight |
| RF | Radio Frequency |
| RMS | Root Mean Square |
| Rx | Receiver Antenna |
| Tx | Transmitter Antenna |
| UOSM | Unknown-Open-Short-Match |
| UWB | Ultra-wide Band |
| VNA | Vector Network Analyzer |

# List of Figures

# List of Tables

# 1 Introduction

In recent years, a growing interest has been directed toward the application of wearable electronic devices in the health care industry. Wearables play a great importance in tracking people's activity for various applications, ranging from fashion to health care. These devices are categorized as body area networks (BANs), where the transmitting and receiving parts are either both placed on the body (on-body link) or one part is placed away from the body (off-body link) [1]. For healthcare applications, a dedicated medical body area network (MBAN) frequency spectrum is allocated by the US Federal Communications Commission (FCC) and the European Commission (EC) [2, 3]. MBANs are networks of low-power wearable sensors which measure physiological parameters and are capable of communicating with a controller device through a wireless link. MBAN devices are mainly used for continuous patient monitoring in health care facilities. During various stages in the development phase of these MBAN devices, knowledge of the radio wave propagation channel as well as the characteristics of the wearable sensor antennas is important. For the purpose of characterizing this knowledge, a good channel model considering the usage of the device is needed.

Channel models for BAN consider the effect of the human body on the radio wave propagation and antenna characteristics. The human body may obstruct and attenuate the radio wave signal, or introduce small scale fading as a result of the coherent addition of creeping waves propagating around the body. The antenna radiation pattern and efficiency, resonance frequency, and input impedance are also affected by the body; therefore, antennas for on-body use should be designed accordingly. It is believed that when modeling such channels, statistical models [4, 5] are more suitable than deterministic models because of the high dynamicity and variability of the channel. These statistical models are usually developed by performing extensive measurements based on intended device use cases which specify antenna placement and body movement. Indoor propagation models are also necessary to characterize the channel based on room sizes and building materials. Therefore, a combined

model which characterizes the effects of the human body as well as the surrounding environment is a scientifically appropriate approach to accurately characterize the MBAN channel.

## 1.1 Motivation

The motivation for this thesis is the investigation of a wireless patient monitoring system using MBAN [7, 8]. The assumption of the system is to provide mobility and comfort to patients by excluding the use of cables for data transmission to monitoring devices that are located away from the body. It also enables an easy transfer of patients to different hospital wards. The system utilizes multiple wearable sensors which are attached to the human body. These sensors are controlled by an external central device through a wireless link for data collection and aggregation. The way the MBAN devices are positioned and the body activities define the general use cases of the MBAN device.

Use cases comprise possible placement of the sensor antenna on the body, body posture, and body movement. Sensor antenna can be placed on the wrist or on the chest. Body posture indicates the patient's physical position, for example, if the patient stands, sits, or lies down in bed. The use cases relevant to the wearable patient monitoring system are different combinations of the above cases. All these activities affect the wireless channel in different ways, requiring specific studies of each use case and their combination for proper channel characterization.

### 1.1.1 Problems

A previous study on BAN has been performed for example, by the IEEE 802.15.6 group [4] for developing a channel model covering in-body, on-body, and off-body links. The model relevant to the MBAN device testing is the off-body channel model. This model generally characterizes the path loss of BAN devices by considering possible shadowing which results due to the body posture or obstacles near the human

body. Unfortunately, the model does not separately characterize the multipath fading caused by the environment from the body shadowing. In addition, the model is based on measurement in one room, and does not represent the effect of a room size on MBAN device performance. Thus, an improved model is required for accurately representing the MBAN channel.

## 1.2 Goal and contents of the thesis

This thesis develops a methodology for testing an MBAN device performance, through developing an improved channel model taking into account the use case and room size. The thesis work has been divided into three main parts: radio channel measurements of use cases, post-processing of the measured channels, and channel modeling and implementation. Chapter 2 provides the theoretical background on wireless channel characterization and survey on BAN channel models. A detailed description of the defined use cases, the conducted channel sounding, and the data processing is given in Chapter 3. Furthermore, Chapter 4 provides results and discussion, including the proposed channel model and its validation. Finally, Chapter 5 concludes the thesis and indicates possible future approaches to improve the proposed methodology.

# 2 Theoretical Background

This chapter summarizes the basic principles of the radio wave propagation mechanisms and wireless channel characterization. It also surveys the relevant literature on channel models.

## 2.1 Propagation mechanisms

An antenna is considered the main component of a wireless communication, as it interfaces the radio frequency (RF) circuitry to a free space [9]. Accordingly, it does this by converting guided waves into propagating waves. In fact, any conductor with a time varying current source will radiate, however antennas are designed to maximize the radiation efficiency. The simplest ideal antenna, an isotropic antenna, radiates equally in all directions having a directivity equal to 1, nevertheless, real application antennas are designed to radiate in a specific direction, thereby increasing the gain. Once radiated from the transmitting antenna, the propagating electromagnetic (EM) wave is subject to different environments which defines boundary conditions. This section will discuss these different propagation mechanisms as well as their implications to the wireless communication link.

### 2.1.1 Free space propagation

In wireless communication, the term free-space is used to express an isolated link between transmit and receive antennas, whereby there is no interacting object which obstructs their clear line of sight (LOS) path. Consequently, in free-space the electromagnetic waves generated with an isotropic antenna radiate equally in all directions. Furthermore, the received power at a distance $d$ away from the transmitting antenna has a spherical spreading loss factor of $d^2$ [10]. This is illustrated by the Friis transmission formula shown in (1) which gives the available received power $P_{RX}$ based on the transmitted signal power $P_{TX}$, wavelength $\lambda$, and gain of antennas $G_{TX}$ and $G_{RX}$ as

$$P_{RX}(d) = P_{TX} G_{TX} G_{RX} \left( \frac{\lambda}{4\pi d} \right)^2 . \tag{1}$$

The antenna gain depends on the antenna aperture as given by (2),

$$G_{RX} = \frac{4\pi}{\lambda^2} A_{RX}. \tag{2}$$

The term $(\frac{\lambda}{4\pi d})^2$ is considered as the free space loss. The Friis equation also holds true for plane waves, where the transmitter (Tx) - receiver (Rx) separation distance has to be greater than the far field distance of the transmitter and receiver antennas such that (1) is valid. The far field distance is defined as $\frac{2D^2}{\lambda}$, where $D$ represents the longest dimension of the antenna perpendicular to the direction of observation. From (1) it is intuitive to suspect a decrease in received signal strength as frequency is increased. However, it is not true if we consider the receiver antenna aperture to be constant over frequency as evident from substituting (2) into (1), therefore, making $P_{RX}(d)$ independent of $\lambda$. The main assumptions taken with the Friis transmission formula are, antenna alignment, polarization and impedance matching, and LOS condition [11]. Nonetheless, in reality all these assumptions are not always met, thus the losses caused by these mismatches must be accounted by including the matching and polarization efficiency parameters ($q$, and $p$ respectively) as shown in (3),

$$P_D(d) = P_{TX} G_{TX} G_{RX} pq \left(\frac{\lambda}{4\pi d}\right)^2. \tag{3}$$

### 2.1.2 Indoor propagation

In contrast to the free space, where the EM wave propagates in LOS, in indoor environment the electromagnetic wave is subject to obstructions. Generally, in this condition the EM wave propagates in four main mechanisms: reflection, transmission, scattering, and diffraction [9].

As discussed in the previous section, one of the assumptions with the free space propagation was the arrival of only LOS component to the receiver antenna. However, the wave follows multiple paths to reach the receiver antenna. When the EM wave is incident on a smooth surface which is much larger than the signal wavelength, it is subject to reflection and transmission. Furthermore, the amount of reflected and transmitted signal is represented by the reflection and transmission coefficients. Figure 1a illustrates the phenomena when an EM wave is incident on an infinite

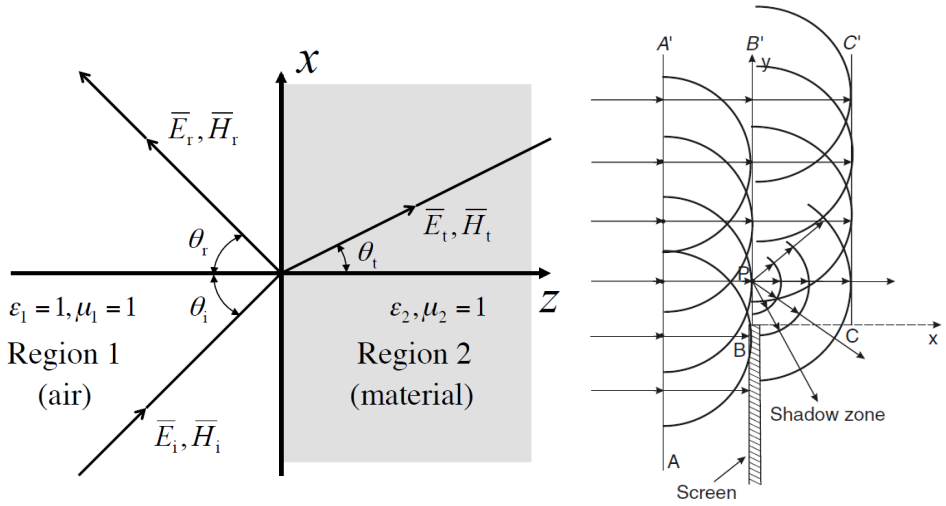


(a) Reflection & transmission

(b) Diffraction

Figure 1: Reflection and diffraction [10]

smooth surface, showing the incident, the reflected, and the transmitted fields. The relation between the incident and reflected waves is given by Snell's law, derived by using the boundary conditions of Maxwell's Equations, which states that the angle of incidence is always equal to the angle of reflection, given by $\theta_i = \theta_r$. The amplitude and phase of the reflected and transmitted waves are different from the incident wave. Though, the sum of the power of the reflected and transmitted waves should be equal to the power of the incident wave on the boundary of the two materials. In addition, as a result of the difference in the dielectric constants of the propagating mediums $(\epsilon_1, \epsilon_2)$, the transmitted signal propagates with a different velocity. This phenomenon is described by Snell's law of refraction denoted as

$$\frac{\sin\theta_i}{\sin\theta_t} = \frac{n_2}{n_1}, \tag{4}$$

where $n_1$ and $n_2$ are the indices of refraction for medium 1 and 2 respectively. Depending on the radio frequency, floor, walls, ceiling, and furnitures with smooth surfaces can be good examples of causes of reflection and transmission in indoor environments.

The third propagation mechanism, scattering, occurs when the EM wave is incident on a rough random surface, with the dimension of roughness being smaller or comparable

to the wavelength. In scattering the incident wave is dispersed in all directions, and might appear as a noise to the receiver. In addition, the polarization of the wave is subject to change in scattering. The surface roughness is described using the perturbation and the Kirchhoff theory which gives a critical height for a given angle of incidence [11] as

$$h_c = \frac{\lambda}{8\sin\theta_i}. \tag{5}$$

A surface with a depth of roughness $h$, smaller than $h_c$ is considered a smooth surface, whereas, a surface with $h$ higher than $h_c$ is considered a rough surface. For instance, indoor plants, book shelves, window frames, furniture and fixtures are good examples of scatterers depending on the radio frequency.

Moreover, EM waves propagate by the means of diffraction when a part of the propagating wave is obstructed by a material. This propagation mechanism is explained by the Huygens principle which states that each point of a propagating wavefront can be considered as secondary sources of a spherical wave. If we consider the simplest case of diffraction with semi-infinite absorbing screen partially obstructing the incident wave [10] as shown in Figure 1b, the diffracted field is represented as a cylindrical wave illuminating the shadow region dictated by the diffraction coefficient.

Fresnel zones are elliptical geometries with the receiver and transmitter antennas as

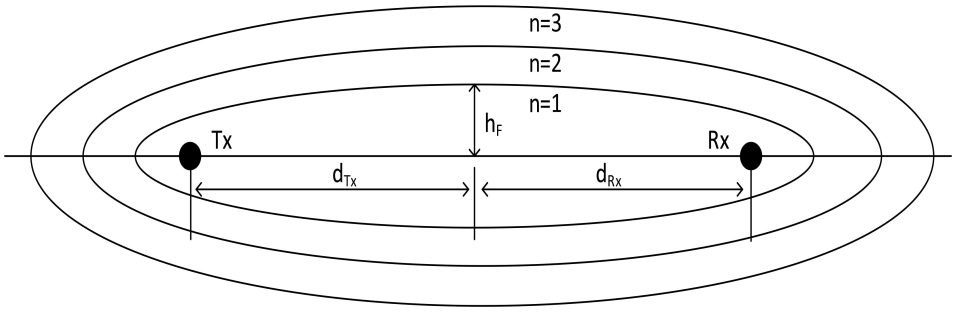


Figure 2: Fresnel zone

foci points as shown in Figure 2. The height of ellipses at the center of the Tx - Rx link is calculated as

$$h_F = \sqrt{\frac{n\lambda d_{\mathrm{Tx}} d_{\mathrm{Rx}}}{d_{\mathrm{Tx}} + d_{\mathrm{Rx}}}}. \tag{6}$$

The Fresnel zone is an important tool in analyzing link performance in wireless communication as it shows about 60% of the power of the propagating wave is confined in the first Fresnel zone. This means, though objects that are located outside the Fresnel zones may result in additional reflected, diffracted, or scattered contributions of radiated energy to the receiver, they cause small distortion. In contrast, objects located inside the Fresnel zones, especially the first zone, may cause significant distortion to the received signal. Diffraction is also known to alter the polarization of the propagating wave if caused by conducting and dielectric screens.

### 2.1.3 Propagation through and around the human body

In MBAN device usage, the knowledge of the effect of the human body on the radio wave propagation is of importance. Depending on the signal strength and frequency, radio waves can propagate through, on or around the human body. When modeling the human body in wireless communication, it is important to consider the body as a lossy dielectric material [12]. The human body is composed of different organs with varying dielectric constants. Thus, an incident signal on a human body is subject to reflection, scattering, diffraction, and transmission. The radio wave propagation inside or around the human body can be divided into two parts; the in-body propagation and on-body propagation.

To analyze the in-body propagation, the most relevant propagation mechanism is the transmission through the human body. Inside the human body, the signal weakens as a result of increase in complex dielectric constant, thus the received signal on the opposite side of the body is highly attenuated. The level of attenuation depends on the operating frequency, body parts, body composition and thickness [13].

On-body propagation can become dominant when a considerable amount of the incident wave is not capable of penetrating the human body. The on-body propagation can be considered as a cumulative effect of surface wave propagation, reflection, scattering, and diffraction. Surface wave propagation is observed when the conductivity of the tissue and operating frequency is high. This mechanism of propagation is dominant in on-body links, where both transmit and receive antennas are placed on

the body [13]. In addition, diffracted and scattered waves from one part of the body may contribute to the received signal on the other part of the body. The dominant factor in off-body propagation is diffraction. When the body is blocking the LOS path, diffracted fields from the lit side of the body illuminates the shadowed region [14].

Furthermore, the human body significantly influences the antenna parameters when the antenna is attached to the body. This direct on-body placement of the antenna will affect the antenna matching and radiation pattern, usually in a negative manner, due to a dielectric loading [15]. In addition body movement will cause polarization mismatch due to antenna misalignment.

## 2.2 Channel characterization

A wireless channel is usually characterized in different ways depending on its behavior. The most general classification of wireless channels is based on time variability and channel bandwidth, where we have time invariant and variant channels, as well as narrowband and wideband channels [16].

The wireless channel is often represented with a channel gain, a power ratio of the received signal to the transmitted signal. As discussed in the previous section, the transmitted signal may follow different propagation mechanisms depending on the environment, and in most cases it is too complicated to describe every mechanism which contribute to the received power. Instead, the wireless channel is usually described with a probability that the channel gain reaches a certain value. Figure 3 depicts the received power as a function of Tx - Rx separation distance, where we can see it can vary strongly on different spatial scales of distance. The fluctuation over very short distance (insert in Figure 3) is called the small scale fading. Whereas, the slower fluctuation of the local-averaged power, which occurs over a larger separation distance, is called the large scale fading or shadowing. Finally, the large scale mean power which depends monotonically on the Tx - Rx separation distance is called the mean path loss [10]. Therefore, the channel gain can be seen as a combination of

three modeling components; the mean path loss, slow fading, and fast fading. The mean path loss monotonically decreases as the Tx - Rx distance is longer, whereas small and large scale fading is described statistically.

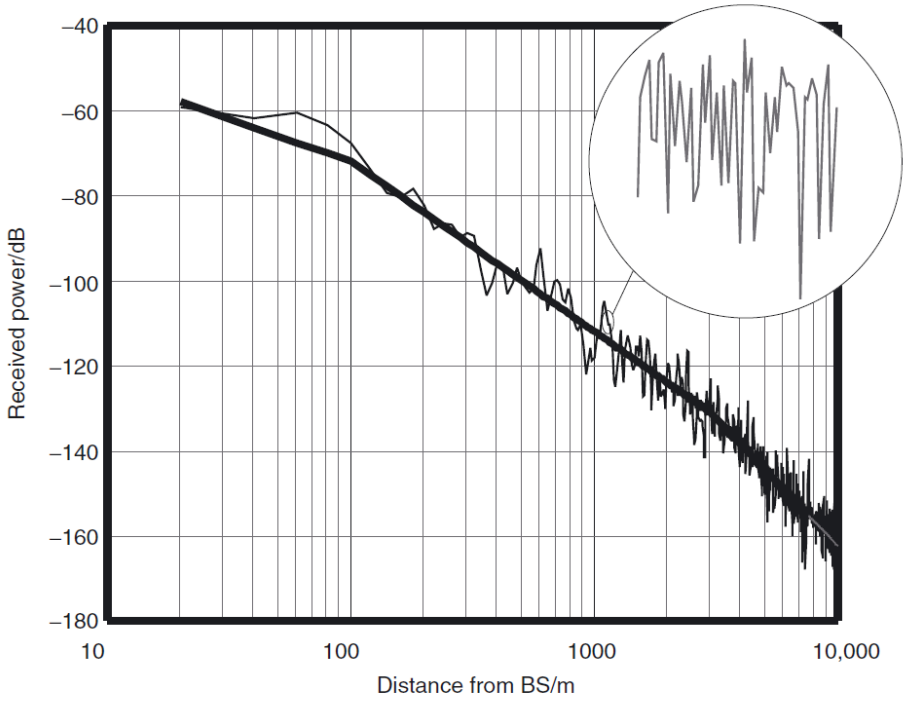


Figure 3: Received power as a function of distance [10]

### 2.2.1 Path loss

Regardless of their behavior all channels are subject to a dominant loss factor which mainly depends on the Tx - Rx separation distance, i.e, the mean path loss. Hence, it is considered as the baseline of link budget estimation in wireless communications. As shown in the free space propagation section, the mean path loss is usually monotonically decreasing with distance . Likewise, it is generally represented as a log function of distance with a path loss exponent $n$ as

$$L_P(d)_{[\mathrm{dB}]} = L_P(d_0)_{[\mathrm{dB}]} + 10n\log_{10}\left(\frac{d}{d_0}\right). \tag{7}$$

The path loss exponent $n$ depends on the surrounding environment and clutter conditions. In free space propagation, the path loss exponent $n$ is 2 as the spreading

of the radiated wave in space. For outdoor propagation, $n$ has a value greater than 2 mainly because the multipath components (MPCs) are much stronger than the LOS component particularly at larger propagation distances. However, in indoor propagation, $n$ can have a value both below and above the free space value [9]. In general the path loss exponent can be smaller than the free space value in a guided wave scenario, where the radiated wave is not actually spreading in all directions but is guided in a certain direction. This phenomenon is often observed in street canyons and indoor corridor propagation. Finally, it is worthy to notice that the path loss exponent, $n$ also depends on antenna heights in some propagation environment, such as urban microcells [17, 18].

### 2.2.2 Shadowing

Shadowing, also known as large scale fading, is a slower fluctuation of the received signal which is observed after the received signal is averaged in local regions. This fluctuation statistically shows a normal distribution in the logarithmic scale. Thus, it is usually described by the lognormal distribution whose probability density function (PDF) is given by [10]

$$pdf_F(F) = \frac{20}{\ln(10) F \sigma_F \sqrt{2\pi}} \exp\left(\frac{(20\log_{10}(F) - \mu_{\mathrm{dB}})^2}{2\sigma_F^2}\right). \tag{8}$$

During an MBAN device usage, body shadowing is observed, especially when the body is moving and either the whole body or some body parts are shadowing the sensor antenna.

### 2.2.3 Small scale fading

Small scale fading occurs as a result of the difference in the phases of MPCs in the received signal. The phase is dependent on the length of the path and the radio frequency [19]; therefore, the small scale fading can be observed both in the frequency and time domains. The main factors influencing the small scale fading are: multipath propagation, a speed of the receiver, a speed of surrounding objects, and

transmission bandwidth of the signal; [11] divides the small scale fading in two major parts depending on the system's bandwidth, i.e, the flat and frequency selective fading. MBAN systems are usually prone to flat fading, since the channel bandwidth is narrow and the frequency response of the channel is almost constant and hence are called narrowband systems. Whereas, systems which experience more often the frequency selective fading mainly because the channel is wideband, are called wideband systems. A second classification of small scale fading can be made based on the frequency of occurrence of deep fades on the time domain when a mobile moves or the environment changes. This time domain phenomenon can be observed in either flat or frequency selective fading channels [20].

Statistical description of the fading channel is given in two separate cases where there is a clear LOS path to the receiver or the LOS is fully blocked by obstacles. When the receiver does not have a clear LOS to the transmitting antenna or the received signal has no dominant multipath component, the amplitude of the faded signal is statistically represented as a Rayleigh distribution. The Rayleigh distribution is represented by its PDF [10]

$$pdf_r(r) = \frac{r}{\sigma^2} \exp\left(\frac{-r^2}{2\sigma^2}\right). \tag{9}$$

In addition, its cumulative distribution function (CDF) is the integral of the PDF and is given as [10]

$$cdf_r(r) = 1 - \exp\left(\frac{-r^2}{2\sigma^2}\right). \tag{10}$$

Conversely, if a strong LOS or specular component is present in the received signal, the fading phenomenon is described statistically with a Rician distribution. The PDF of the Rician distribution is given as [10]

$$pdf_r(r) = \frac{r}{\sigma^2} \exp\left(\frac{-r^2 + A^2}{2\sigma^2}\right) I_0\left(\frac{rA}{\sigma^2}\right). \tag{11}$$

The ratio of the dominant LOS component to the other multipath component is represented with the $K_r$ value, called a K-factor of the distribution as

$$K_r = \frac{A^2}{2\sigma^2}. \tag{12}$$

A high K-factor value represents a dominant signal in the receiver, whereas a low K-factor value means no dominant component is present and the fading approximates Rayleigh fading.

A Nakagami-m distribution is also widely used to describe small scale fading in wireless communication. Its PDF [10] is given as

$$pdf_r(r) = \left(\frac{2}{\Gamma(m)}\right)^2 r^{2m-1} \exp\left(\frac{-m}{\Omega}\right) r^2, \tag{13}$$

where $\Gamma(m)$ is the Euler's Gamma function, $\Omega = r^2$, and $m = \frac{\Omega^2}{(r^2-\Omega)^2}, m > 1$.

The relation between the Rician K-factor and the Nakagami $m$ is given in [21] as

$$K_r = \frac{\sqrt{m^2 - m}}{m - \sqrt{m^2 - m}}. \tag{14}$$

Studies show that most of the times the small scale fading in BANs is represented with Rician fading, as there is a dominant LOS or multi path component in the received signal.

### 2.2.4 Delay dispersion

In channels which exhibit frequency selective fading, the received power varies over a given frequency range. In indoor propagation, the main causes of this variations are: reflections from floor, ceiling, and walls; as well as diffraction and scattering from furniture and clutter. Usually, this variation is explained in the delay domain where MPCs arrive to the receiver after a certain delay; thereby, causing a dispersion of the received power in the delay domain. Furthermore, the delay of arriving MPCs is related to the relative position of the ceiling, floor, or walls from the receiving antenna. The relative powers of the MPCs are specified by the power delay profile (PDP) of the channel, which is defined as the variation in the mean power of the channel with delay $\tau$ [9] as

$$P(\tau) = \frac{E\left[|h(t,\tau)|^2\right]}{2}, \tag{15}$$

where $E$ stands for the ensemble average and $h(t,\tau)$ is the channel impulse response of a time-varying channel. The PDP can be characterized by various parameters

such as the total excess delay, mean excess delay, and root-mean-square (RMS) delay. The RMS delay spread is the square root of the second central moment of the power delay profile [11] and is given as

$$\sigma_\tau = \sqrt{\overline{\tau^2} - (\overline{\tau})^2}, \tag{16}$$

where

$$\overline{\tau^2} = \frac{\sum_k P(\tau_k^2)\tau_k}{\sum_k P(\tau_k)}, \tag{17}$$

and $\overline{\tau}$ is the mean excess delay defined as

$$\overline{\tau} = \frac{\sum_k P(\tau_k)\tau_k}{\sum_k P(\tau_k)}. \tag{18}$$

The RMS delay spread is a better indicator of link performance mainly because it considers both the delay of taps and their relative powers. It indicates the system error rate performance where an RMS delay spread much smaller than the symbol length implies no significant inter-symbol-interference (ISI), or conversely larger RMS delay spread implies the occurrence of ISI. This phenomenon occurs when the symbol arrives to the receiver with the transmitted duration plus the delay, thus causing interference with the next symbol. Similar observation can be done from the frequency domain by comparing the coherence bandwidth of the channel with the bandwidth of the system. The coherence bandwidth is defined from the frequency correlation function, which shows how instantaneous fading realizations are correlated at different frequencies, as the frequency separation where the correlation equals 0.5. The coherence bandwidth also defines the frequency range where frequency-flat fading may hold. In addition, the time varying nature of the channel is described by the coherence time; a parameter which measures the time duration over which two received signals have strong amplitude correlation.

In indoor propagation delay dispersion is related to the room volume as explained by the theory of room electromagnetics [6]. The receiver antenna will receive a dominant LOS component plus diffuse component from MPCs. The reverberation time; defined as the time taken for the diffused field to drown in the noise floor is shown to depend on the room volume and absorption area. The reverberation time

also indicates whether ISI can occur or not. At smaller Tx - Rx distances the LOS component is strong, but as the distance increases the diffuse components will start to dominate and the LOS component weakens. The distance at which the two powers become equal is called the reverberation distance, where at smaller distance the LOS dominates and for larger distance the diffused energy dominates. The reverberation distance is also a function of the room absorption area.

## 2.3 Channel models

In general channel models are used for the design and optimization of radio links. Based on the method of developing the models, they are mainly divided into two groups; deterministic and stochastic models. Deterministic models are based on solving Maxwell's equations or its high-frequency approximations and are relying on numerical computation [16, 10]. Whereas, stochastic models are developed based on measurement campaigns to provide statistical description of the wireless channel [4]. In some applications there also exist a hybrid channel model which is developed by combining the two channel models, for example where Ray tracing has been aided with measurement results to increase the accuracy of the model [22]. This section provides the relevant literature survey on channel models developed for indoor BAN applications.

### 2.3.1 Deterministic models

The simplest deterministic model is the free space path loss model. It is a model for the mean received power which have been averaged both over large and small scale fading, and is represented with the log-distance function as in (7). A realistic and still fairly simple model is the two ray model, which considers the reflected signal from a large flat ground in addition to the LOS component [23]. It is a widely used simplified model mainly for outdoor applications. Ray tracing is based on high-frequency approximation of Maxwell's equations that uses rays [10]. This model requires accurate geometric information of the surrounding environment and is

usually used both for outdoor and indoor applications. A more complex deterministic modeling methods include the finite difference time domain (FDTD) [24] and the method of moments (MOM) [25], which require high power of computation.
Deterministic models in BANs are usually developed based on the FDTD method. These models cover the in-body and on-body communications. The off-body channel characterization is usually modeled in a hybrid manner by combining simulation results with measurements [26, 27, 28, 29]. Deterministic BAN channel models have been developed, for example, in [30, 31]. Most channel models are capable of reproducing the path loss, the slow fading, and the fast fading components.

### 2.3.2 Stochastic models

BAN channel models consider three different types of channels based on the location of the communicating devices. These include the on-body, the in-body, and the body-to-body or off-body channels. The on-body channel considers the nodes at the ends of the communication link to be placed on the human body. In this case the main propagation mechanism followed is diffraction, creeping waves on the body, or LOS. The in-body channel considers implanted device communicating with another device which is either implanted or placed on the body. In body-to-body or off-body channel one of the nodes is placed on the human body, whereas the second can be either placed on another human body or off the body. In these cases the free space propagation component is also considered in addition to the on-body propagation mechanisms.
The IEEE 802.15 Task group 6 [4] has been formed in order to standardize BANs' PHY and MAC layers that are optimized for short-range in-body, on-body, and off-body transmission. The standard could be applied for medical and non-medical applications. Since the range of applications which BANs cover is broad, the Task group divides their focus based on the frequency allocation as: Human Body Communication, narrowband at multiple center frequencies, and Ultra-wide Band (UWB) (3.1-10.6 GHz). The IEEE 802.15.6 group has divided BANs in to 7 scenarios (S1 - S7) where S1 covers implant-to-implant, S2 and S3 are for implant-to external devices (CM2),

S4 and S5 for body-to-body communications (CM3), and S6 and S7 for off-body communications (CM4). The nodes are classified as implant, body surface, and external node. The standard also provides a channel model for different scenarios including the effect of the environment and the body posture. Figure 4 illustrates the scenarios which are covered in the IEEE 802.15.6 channel model. It is difficult to derive a simple path loss model for BANs as the human body is a lossy component consisting of different organs with different electrical characteristic. In addition the operating frequency influences the amount of loss or penetration to the body.

As the focus of the thesis is on off-body channels, we will briefly survey the IEEE

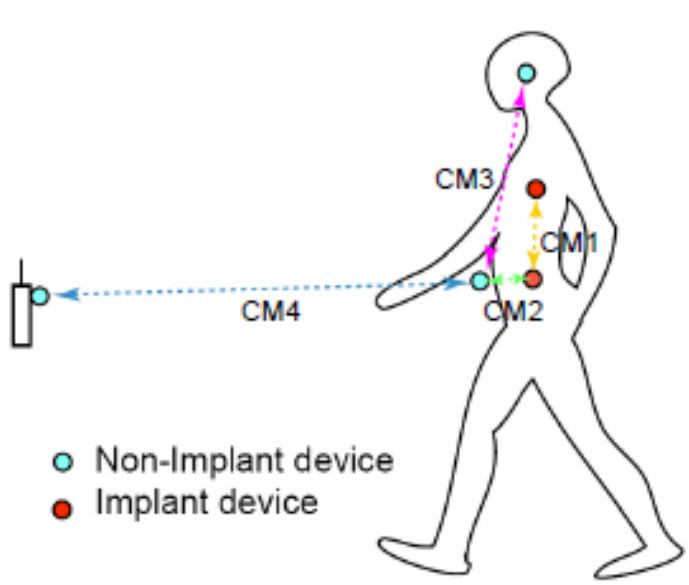


Figure 4: IEEE 802.15.6 channel models [4]

802.15.6 CM4 channel model hereinafter. The CM4 channel model covers the body-surface to external scenarios both for narrowband [32] and UWB [33] channels. These models address mobile and stationary scenarios as well as the impact of nearby objects. The narrowband channel measurements were performed at 900 MHz and 2.36 GHz ISM bands covering a 10 MHz bandwidth. Two antenna locations on the body were investigated: on chest and on wrist; where the test subject is standing or walking on spot, facing in four different directions, at 1, 2, 3, or 4 meters away from the off-body receiving antenna. A significant effect on the path loss has been

noticed as a result of body orientation. In particular, a greater path loss, on average 7 dB and up to 19 dB, was measured during none-line-of-sight (NLOS) condition as compared to LOS conditions. Furthermore, the path loss variation observed while stationary was at most 4 dB, and increased up to 24 dB when walking. The average variation was higher in the wrist position than in the chest position, because the wrist has a larger range of movement. In addition, the received power for all scenarios was normalized and statistically described using various distributions. In general, the normalized-received power followed a lognormal distribution.

Separate measurements have also been performed to characterize the channel when the person is in a sleeping position in a bedroom. In this scenario, the normalized-measured channel gain followed a Gamma distribution with parameters $a = 3.00, b = 0.29$ for antenna placed on the right wrist. Different signal strengths were measured during sitting and standing body postures as well. Overall, the IEEE 802.15.6 channel models were developed to evaluate the performance of different physical layer proposals, and are not intended to provide information of absolute performance in different environments or body postures.

Usually, a space-time varying channel model of narrowband BANs [26] assumes the instantaneous received power at a given time and radio frequency as the sum of three main components; the mean path loss, the body shadowing, and the multipath fading from environment as

$$L_{PT}(d)_{[\mathrm{dB}]} = \overline{L_P}(d)_{[\mathrm{dB}]} + \Delta L_{B[\mathrm{dB}]} + \Delta L_{F[\mathrm{dB}]}, \tag{19}$$

where $\overline{L_P}(d)$ is mean path loss, $\Delta L_B$ is body shadowing, and $\Delta L_F$ is multipath fading.

# 3 Research Materials and Methods

This chapter lists the materials and methods that have been used in the thesis. It starts with the use case definition and description of the measurement environments, and continues to list the measurement equipment used for channel sounding. The last section explains the data processing method following the measurements.

## 3.1 Measurement scenario

Five use cases, U1 to U5, which are of relevance to practical MBAN deployment have been selected for investigation. These use cases are illustrated in Figure 5. All use cases consider the sensor (Rx) antenna attached to the wrist while the hub (Tx) antenna is located away from the body at a given separation distance. The first two use cases, U1 and U2, consider a patient, wearing the sensor (Rx) antenna, to stand still or walk on spot at 1, 2, 3, and 4 meters distance from the Tx antenna. Whereas, in U3 a continuous walk in a maximum of 4m distance away from the Tx antenna is considered. The last two use cases, U4 and U5, consider a patient wearing the sensor antenna to lie down on a bed, while the Tx antenna is placed 1m away from the bed.

Table 1: Considered use cases

| Use case | U1 | U2 | U3 | U4 | U5 |
|---|---|---|---|---|---|
| Action | Stand | Walk on spot | Real walk | Lie on bed | |
| Body rotation | 0°, 90°, 180°, 270° | | 0°, 180° | 0°, 90° | |
| Sensor antenna | Right wrist | | | | Left wrist |

Body rotation is considered in all the use cases, where a 90° step rotation from 0° to 270° is performed for use cases U1, U2, and U3 as shown in Figure 6, and $0°, 90°$ rotation is performed in U4 and U5. The Transmitting antenna is placed away from the body at all times and positioned at a height of 1.1 meter above the floor. A summary of the use cases is provided in Table 1.

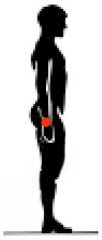

(a) Standing, U1

(b) Walking on spot, U2

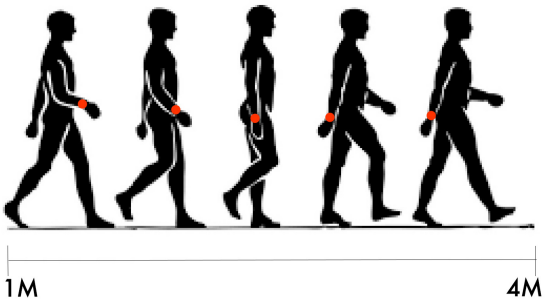


(c) Continuous walking, U3

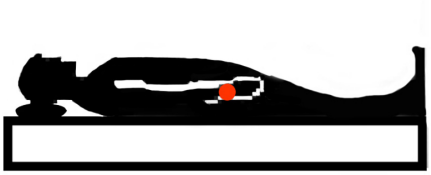

(d) Lying in bed, U4 & U5

Figure 5: Illustration of several use cases, where sensor antenna is attached to the wrist (red dot)

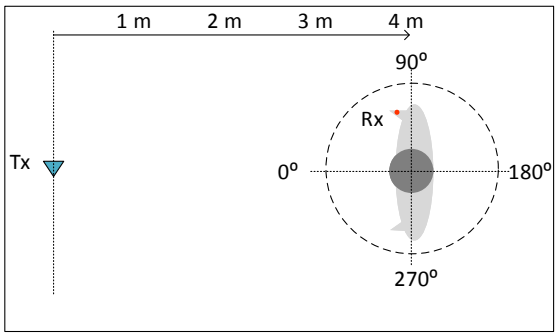


(a) U1 - U3

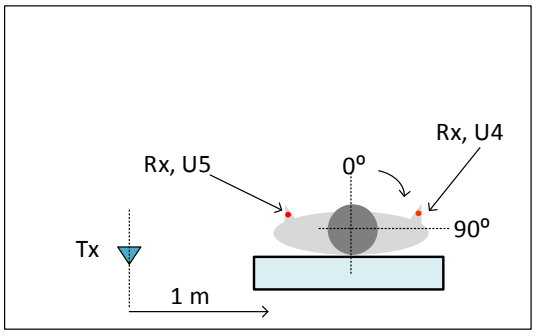


(b) U4 & U5

Figure 6: Body rotation for use cases U1 to U3 (a), and U4 & U5 (b)

Measurements have been carried out in two different environments: the anechoic chamber, where the effect of surrounding environment on the channel is negligible, and an indoor office environment having furniture and other appliances. In particular, measurements for use cases U1 to U3 were performed in an anechoic chamber and two office meeting rooms: Room 1 and Room 2, with different sizes. A description of the measurement environments is shown in Figures 7 and 8. Each measurement set included the case where the sensor antenna was not attached to the body (no-body, NB), but spatially positioned using a fixture, in order to study and separate the effect of body from the room size. The measurement for use cases U4 and U5 were performed in a hospital mock up room, Room 3, with beds and patient monitoring devices as illustrated in Figure 9. In addition, a summary of the measurement environments and the corresponding use cases is provided in Table 2. The reported dimensions of the anechoic chamber are the available inner dimensions.

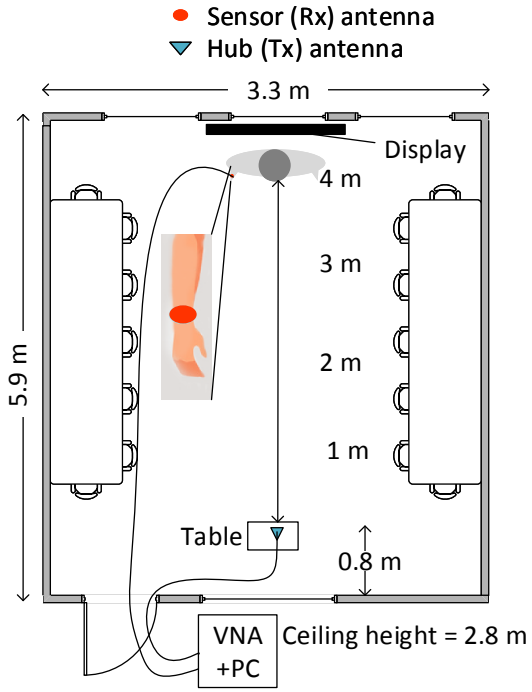


Figure 7: Measurement environment: Room 1

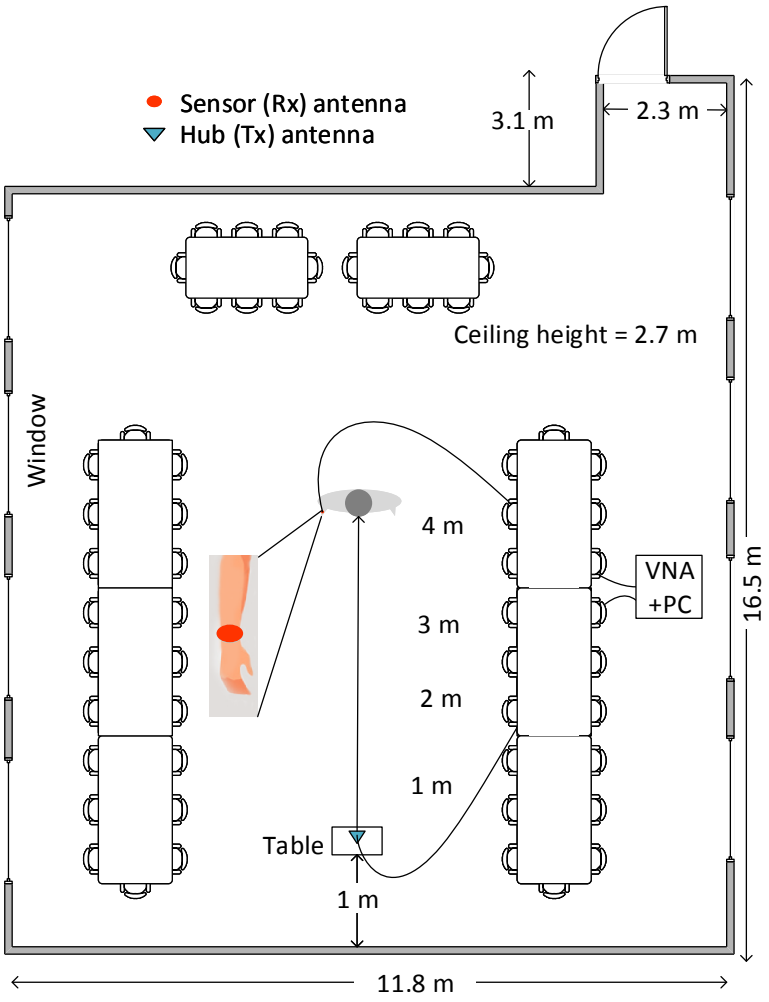


Figure 8: Measurement environment: Room 2

Table 2: Summary of measurement environments and covered use cases

| Environment | Volume [m$^3$] | Covered use cases |
|---|---|---|
| Anechoic chamber | 6.2x3.8x2.4 | U1, U2, U3 |
| Room 1 | 5.9x3.3x2.8 | U1, U2, U3 |
| Room 2 | 16.5x11.8x2.7 | U1, U2, U3 |
| Room 3 | 7.5x6.0x2.8 | U4, U5 |

## 3.2 Measurement equipment

The measurement was carried out by using a Vector Network Analyzer (VNA), ZNB 8; vertically polarized dipole antennas, AIR-ANT2524DB-R; coaxial cables and strap

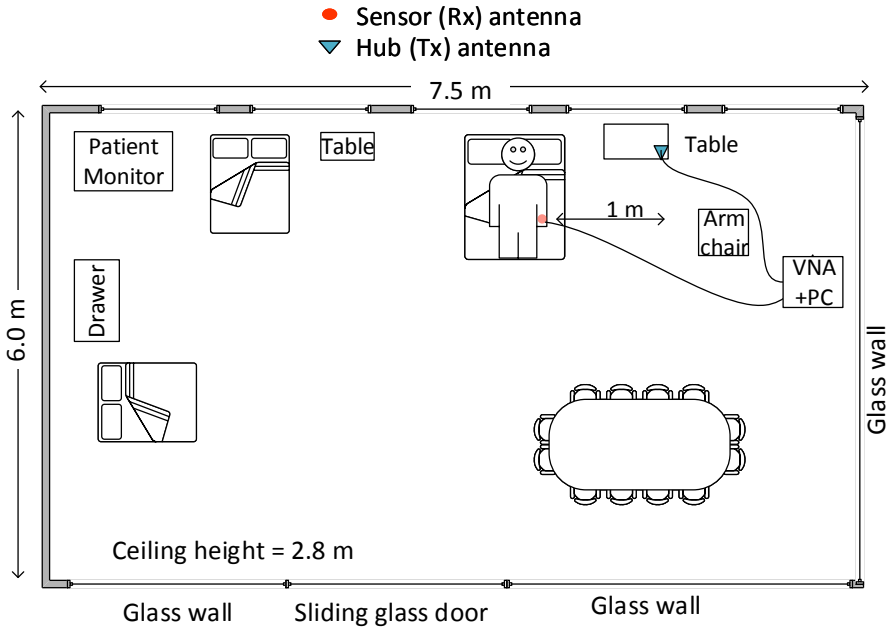


Figure 9: Measurement environment: Room 3

bands for attaching the antenna on the wrist. A male adult person (185 cm/ 89 kg) volunteered to wear the sensor antenna and perform all the use case measurements. The frequency range of the measurement was from 2.3 GHz to 2.5 GHz covering the US MBAN, ISM band, and EU MBAN. The VNA was controlled by a laptop computer through an Ethernet cable using MATLAB [34], for continuously acquiring and storing channel transfer functions over time. The VNA sweeps through 201 points in the given frequency bandwidth in 3.5 ms to measure the channel transfer function ($S_{21}$); 201 time samples of the channel transfer functions over 8 second duration were measured in all use cases except in U3, where 50 second duration were measured for continuous walking. A full Unknown-Open-Short-Match (UOSM) VNA calibration was performed before each measurement set by using a ZN-2153 calibration unit. The resolution bandwidth (RBW) of the VNA was set to 100 kHz. The settings of the VNA during the measurements are shown in Table 3.

The effect of placing the antenna on the wrist has been investigated by measuring the return loss $S_{11}$ of the antenna before and after being attached to the wrist. It can be seen from Figure 10 that the impedance bandwidth of the antenna has actually improved when attached to the wrist, and using this antenna for off-body

measurements is acceptable.

Table 3: VNA settings

| | |
|---|---|
| Frequency | 2.3–2.5 GHz |
| Calibration | Full UOSM |
| Sweep points | 201 |
| Sweep time | 3.517 ms |
| RBW | 100 kHz |
| Tx Power | 10 dBm |

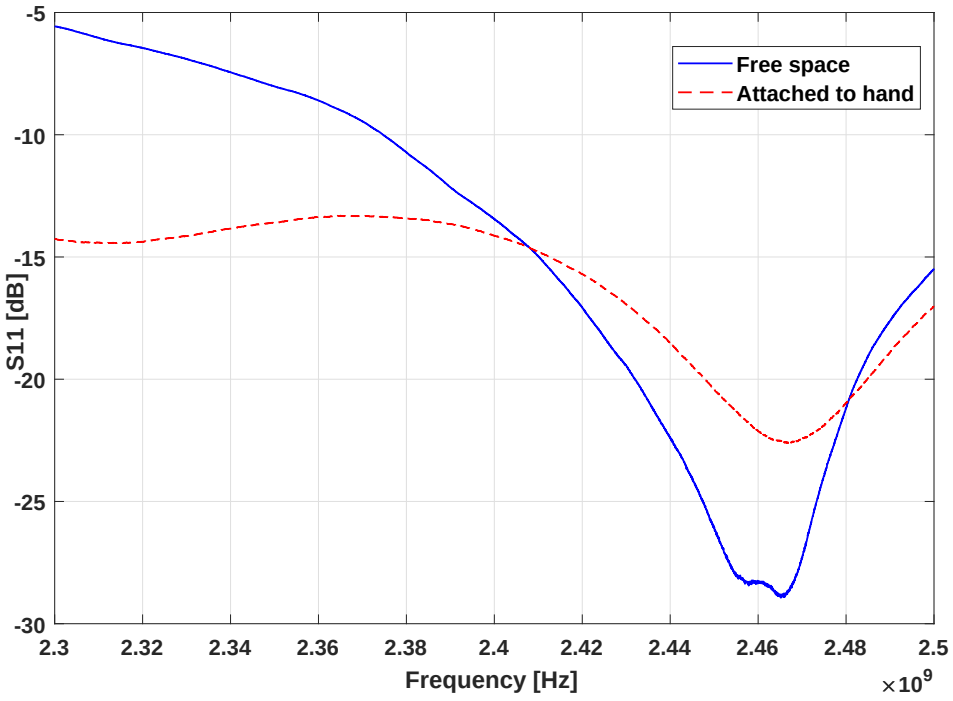


Figure 10: Effect of the body on antenna impedance matching

## 3.3 Data processing

Following the channel sounding, the acquired channel transfer functions of each measurement run were analyzed by using MATLAB. The first step taken during this process was to extract the mean path loss from the instantaneous received power based on (19). For all use cases except U3, this is realized by averaging the received power over the 201 frequency points ($N_f$) and over the 201 time samples ($N_t$) as

$$L_P(d) = \frac{1}{N_t N_f} \sum_{t=1}^{N_t} \sum_{f=1}^{N_f} P_r(d,t,f). \tag{20}$$

For the walking scenario U3, the path loss is estimated by taking a moving average of instantaneous transfer functions over 10 wavelengths of the Rx antenna on the walking route; as being the typical value for indoor environments [35]. Then the mean path loss at each distance is fitted to the log function of distance as

$$L_P(d)_{[\mathrm{dB}]} = \overline{L_P}(d_0)_{[\mathrm{dB}]} + 10n\log_{10}\left(\frac{d}{d_0}\right), \tag{21}$$

where $n$ is the path loss exponent and $\overline{L_P}(d_0)$ is the mean path loss at the reference distance $d_0$. The value of $n$ is computed using linear regression such that the mean square error between measured and estimated path loss is minimized. The goodness of this fit is analyzed with the parameter $R^2$ which is defined as

$$R^2 = 1 - \frac{\sum_{i=1}^{N}(y_i - \hat{y}_i)^2}{\sum_{i=1}^{N}(y_i - \overline{y}_i)^2}, \tag{22}$$

where $\hat{y}$ is the calculated values of $y$, and $\overline{y}$ is the mean of $y$.

Body shadowing is modeled as a lognormal distribution, and their realizations are extracted from the frequency-averaged instantaneous received power by subtracting the mean path loss component as

$$\Delta L_{B[\mathrm{dB}]} = \frac{1}{N_f} \sum_{f=1}^{N_f} P_r(d,t,f)_{[\mathrm{dB}]} - L_P(d)_{[\mathrm{dB}]}. \tag{23}$$

The extracted data is then fitted to a lognormal distribution based on maximum likelihood parameter estimates [36].

The multipath fading is finally extracted by subtracting the mean path loss and body

shadowing components from the magnitude of the instantaneous channel transfer functions. Then the power-normalized multipath fading samples are fitted to a Rician distribution. The Rician K-factor was estimated by the moment estimation method from [37]. The body rotation impact on the Rician K-factor is analyzed by separating the use cases into three channel types; the LOS, quasi LOS (QLOS), and NLOS conditions. For use cases U1 to U3, LOS condition comprise body rotation angle of 0° and 270°, QLOS considers 180°, and NLOS considers 90°, Figure 6. Whereas, body rotation angle of 0° in U5 is considered LOS, 90° in U5 is considered QLOS, and both 0° and 90° rotations in U4 are considered NLOS.

In addition the time-frequency correlation of small scale fading has been analyzed. The correlation is analyzed for the Gaussian components of the Rician channels. The Gaussian component $h_g$ was extracted by subtracting the dominant component $h_0$ from the instantaneous complex channel transfer function $h_T$ as

$$h_g = h_T - h_0. \tag{24}$$

The dominant component was estimated by performing a peak detection in the delay domain over channel impulse responses. The channel impulse response was acquired by using inverse fast Fourier transform (IFFT) of the measured channel transfer functions. Once the peak was detected, $h_0$ was calculated as

$$h_0 = a_0 \exp\left(-\mathrm{j}2\pi f \tau_0\right), \tag{25}$$

where $a_0$ is the peak amplitude, and $\tau_0$ is the time delay of the dominant component. Figure 11 shows an example of this process both in time and frequency domains.

The frequency correlation of the Gaussian component was calculated as

$$\rho(k) = \frac{1}{N_f - k} \sum_{i=1}^{N_f - k} h_g^*(f_i) h_g(f_{i-k}), \tag{26}$$

where $N_f$ is the number of samples over the frequency, $k$ is the frequency interval on which the correlation is calculated such that $k = 1$ is equivalent to 1 MHz. The same method was used to calculate the time correlation by substituting $t$ in place of $f$ in equation (26). In this case, $k$ is the time interval and $k = 1$ is equivalent to 40 ms

Finally, the time dispersion nature of the channel was studied from the power delay profile $P(\tau_k)$ by calculating the RMS delay spread; $P(\tau_k)$ is calculated from the instantaneous measured transfer functions as

$$P(\tau_k) = |\mathcal{F}^{-1}(h_T(d,t,f))|^2. \tag{27}$$

The delay spread has been calculated by using a noise threshold value of $-90$ dB.

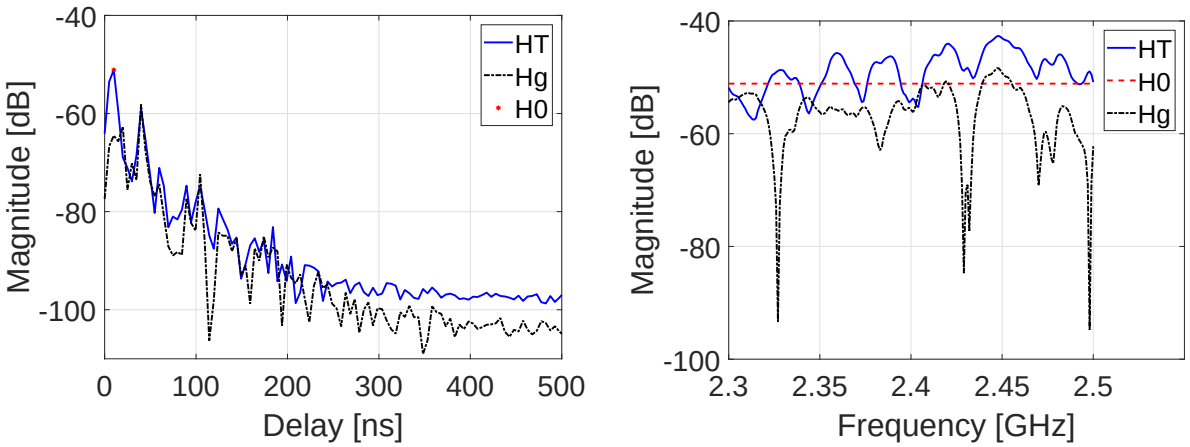


(a) Delay domain

(b) Frequency domain

Figure 11: Illustration of peak detection and separation of Gaussian components in the delay and frequency domain respectively

# 4 Results and Discussion

This chapter covers the obtained results and their respective discussion. It is divided into two sub chapters: the result, and model implementation. The discussion is given in each section.

## 4.1 Results

The raw measured channel transfer functions, prior to their separation into the three components, were observed for a general understanding of their nature. Figure 12 illustrates the observed time-varying channel transfer function of U3 in Room 1. This 3 dimensional graph shows the dynamic nature of the channel over frequency and time domains. During the static use cases, the channel has been observed to be flat over time but was frequency selective because of small scale fading especially in the measurement rooms, Room 1, Room 2, and Room 3. The body rotation has also been seen to increase the frequency selectivity of the channel as the body partially or fully blocks the LOS path. As expected the body movement has caused the channel to be more dynamic and significant fluctuations of the channel gain have been observed over time in the cases of U2 and U3.

### 4.1.1 Path loss

The mean path loss was observed to vary substantially based on body orientation and movement. The measured path loss for all the use cases and conditions are provided in the appendix Tables 12 - 15. Smaller mean path loss value was measured during the 0° and 270° body orientation as compared to 90° and 180° orientation (Figure 6) because of the presence of clear LOS path in 0° and 270° body orientations. The body attenuation was significant in the 90° orientation, where it was up to 30 dB in the anechoic chamber and 8 dB in Room 1. An attenuation higher than 30 dB was observed for the use case U4, where the sensor antenna was completely covered by the body. The diffracted wave around the body is responsible for the reception of signals in the anechoic chamber even when the LOS path was totally blocked by

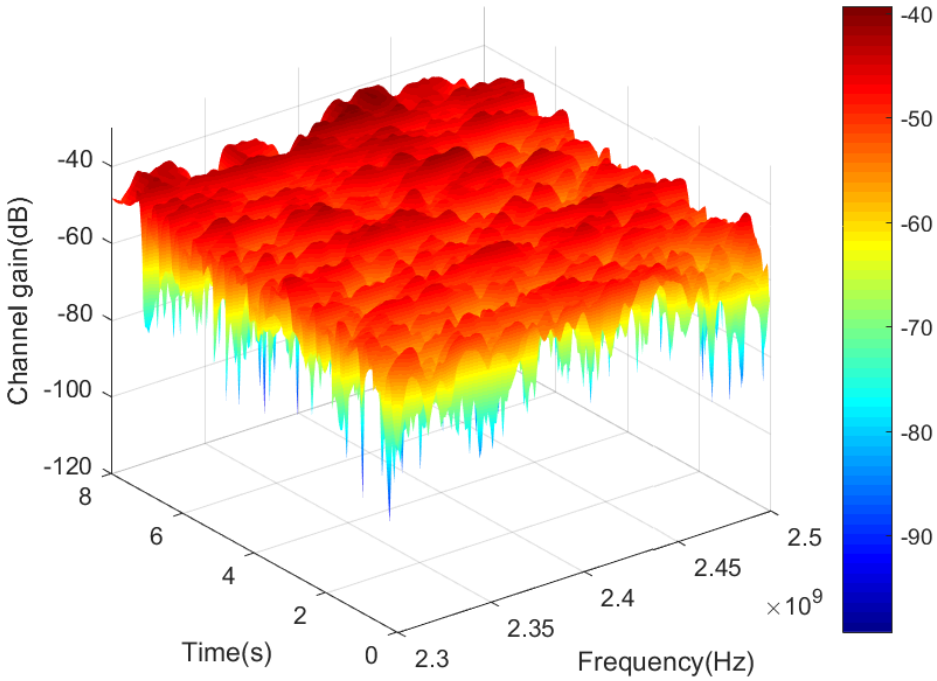


Figure 12: Time-varying channel transfer function, Room 1 , U3

the body. The body movement, where both the legs and hands were moving, has resulted in about 3 dB variation of the mean path loss value. This variation indicates that the effect of movement is also present in the mean path loss value. In U3 the mean path loss was observed to clearly increase with the link distance for the LOS condition, whereas no clear dependence has been observed for the NLOS conditions as the multipath effect was dominating.

The path loss exponent, $n$, mean path loss at the reference distance $L_P(d_0)$, and the goodness of fit parameter $R^2$ are shown for different use cases and the room size in Tables 4 - 6. In general best goodness of fit is obtained for the 0° and 270° body rotations as the LOS path is not obstructed by the body in these cases. However, the body shadowing effect in the remaining two body rotations has resulted in a relatively smaller value of $R^2$ than 1. In the worst case, with the smallest value of $R^2 = 0.03$, the path loss exponent was seen to be below 0, implying that path loss has decreased with increasing distance. This could be a result of the multipath rich

environment, as similar observation has been reported, for example, in [32, 38]. In the measurement rooms $n$ was often smaller than 2 (the free space value) due to multipath [26, 39].

Table 4: Path loss model parameters in Anechoic chamber

| Use case | Rotation | $L_P(d_0)_{[\mathrm{dB}]}$ | $n$ | $R^2$ |
|---|---|---|---|---|
| U1 | 0° | 50 | 1.10 | 0.93 |
| | 90° | 72 | −0.03 | 0.03 |
| | 180° | 64 | 0.97 | 0.90 |
| | 270° | 41 | 2.48 | 1 |
| U2 | 0° | 46 | 2.17 | 0.99 |
| | 90° | 76 | 0.10 | 0.08 |
| | 180° | 59 | 0.48 | 0.51 |
| | 270° | 41 | 2.13 | 1 |
| U3 | 0° | 49 | 1.30 | 0.99 |
| | 180° | 61 | 1.55 | 0.96 |
| NB | 0° | 36 | 2.09 | 0.99 |

The path loss variation based on the room size is illustrated in Figure 13. The figure compares the path loss model parameters for the inverse of electromagnetic reverberation volume of the rooms; where the reverberation volume of the anechoic chamber is assumed to be $\infty$. In general path loss exponent is observed to decrease with decrease of the room size, as expected for indoor propagation [6]. The smaller room can be assumed as a reverberation chamber, allowing many propagation paths to arrive from the transmitter to the receiver. The LOS path loss exponent curve is very similar with the no body (NB) case. For the NLOS case, $n$ is smaller but still decreases with the room size. The reference path loss comparison has not showed a clear pattern over room volume in both LOS and NLOS conditions.

Table 5: Path loss model parameters in Room 1

| Use case | Rotation | $L_P(d_0)_{[\mathrm{dB}]}$ | $n$ | $R^2$ |
|---|---|---|---|---|
| U1 | 0° | 44 | 1.42 | 0.94 |
| | 90° | 52 | 0.25 | 0.22 |
| | 180° | 52 | 0.42 | 0.40 |
| | 270° | 43 | 1.28 | 0.80 |
| U2 | 0° | 49 | 0.92 | 0.92 |
| | 90° | 56 | −0.11 | 0.38 |
| | 180° | 51 | 0.61 | 0.92 |
| | 270° | 41 | 2.11 | 0.98 |
| U3 | 0° | 49 | 0.87 | 0.97 |
| | 180° | 52 | 0.24 | 0.72 |
| NB | 0° | 37 | 1.04 | 0.87 |

Table 6: Path loss model parameters in Room 2

| Use case | Rotation | $L_P(d_0)_{[\mathrm{dB}]}$ | $n$ | $R^2$ |
|---|---|---|---|---|
| U1 | 0° | 40 | 1.84 | 1.00 |
| | 90° | 56 | 1.15 | 1.00 |
| | 180° | 47 | 1.78 | 0.91 |
| | 270° | 37 | 1.96 | 1.00 |
| U2 | 0° | 43 | 1.52 | 1.00 |
| | 90° | 59 | 0.86 | 0.72 |
| | 180° | 43 | 2.26 | 1.00 |
| | 270° | 32 | 3.21 | 0.96 |
| U3 | 0° | 42 | 1.33 | 1.00 |
| | 180° | 56 | 1.17 | 0.99 |
| NB | 0° | 37 | 2.01 | 1.00 |

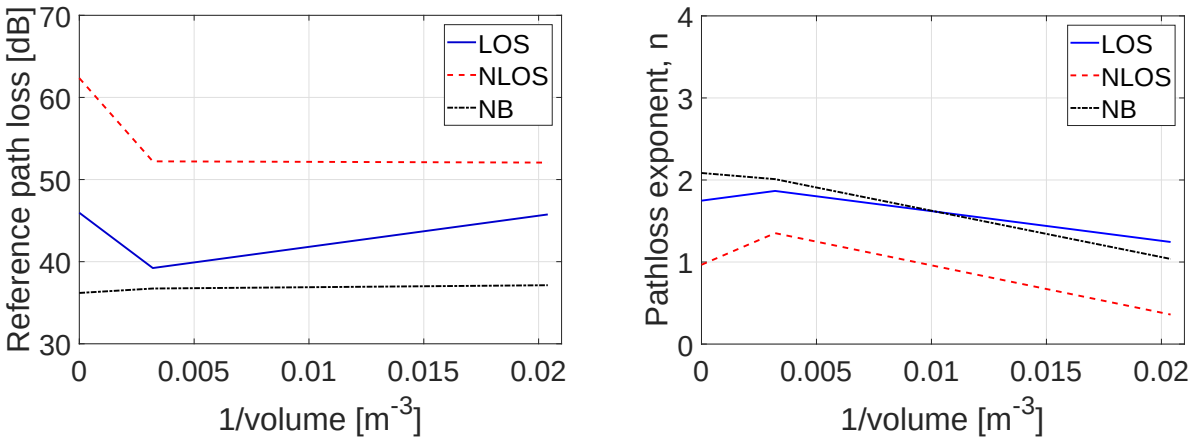


(a) Reference path loss, $L_P(d_0)$

(b) Path loss exponent, $n$

Figure 13: Comparison of reference path loss $L_P(d_0)$ and path loss exponent $n$ for the inverse of room volume in LOS and NLOS conditions

### 4.1.2 Body shadowing

The body shadowing has been analyzed and described by the lognormal distribution. The mean $\mu_{\text{dB}}$ and the standard deviation $\sigma_{\text{dB}}$ of the body shadowing components for each measurement run are reported in the appendix Tables 16 - 18. Here the summarized results are shown in Table 7. In general body shadowing was mainly affected by the body movement and rotation. Higher values of $\sigma_{\text{dB}}$ were observed for U3 where the body was in continuous movement. The mean value, $\mu_{\text{dB}}$ was observed to be close to 0 dB for all the use cases implying the path loss component was extracted appropriately.

Table 7: Summary of lognormal body shadowing model parameters

| Use case | Room 1 | | Room 2 | | Anechoic chamber | |
|---|---|---|---|---|---|---|
| | $\mu_{\text{dB}}$ | $\sigma_{\text{dB}}$ | $\mu_{\text{dB}}$ | $\sigma_{\text{dB}}$ | $\mu_{\text{dB}}$ | $\sigma_{\text{dB}}$ |
| U1 | $-0.02$ | 0.33 | $-0.01$ | 0.16 | 0.00 | 0.23 |
| U2 | $-0.09$ | 0.81 | $-0.05$ | 0.56 | 0.00 | 0.75 |
| U3 | $-0.18$ | 1.24 | $-0.13$ | 1.08 | $-0.11$ | 0.97 |

For static use cases, $\sigma_{\mathrm{dB}}$ was below 0.5 dB for most cases. This is expected as the channel is not considered to be dynamic in these use cases. However, $\sigma_{\mathrm{dB}}$ values close to 1 dB were observed for NLOS cases. The standard deviation has been increased by the body movement to a maximum of 2 dB in NLOS conditions. Results from U3 show $\sigma_{dB}$ ranging [0.88, 1.37] dB. These results are comparable to those reported in [26]. The impact of room size on body shadowing is not clearly observed from Table 7 for U1 and U2 cases. In general the observed $\sigma_{\mathrm{dB}}$ is very small, implying that body shadowing as a result of small movements of the hands and legs for off-body communications is not as significant as the effect of body rotation.

### 4.1.3 Multipath fading

Multipath fading has been analyzed for all the measurements and at first the distribution that best fits each case was checked. The distributions compared were: the Rician, Nakagami, Rayleigh, Lognormal, Gamma, Weibull, and Normal. The full description of the best-fit distribution for all the measured use cases is shown in the appendix Tables 19 - 22. It was seen that the Rician distribution was the best fit for almost all the dynamic and majority of U1 measurements in Room 1. The Rician distribution was not the best fit for the majority measurement runs in Room 2 and anechoic chamber, but it was still a reasonable fit. As there was no common best-fit distribution for all the use cases and the Rician distribution was seen among the first three best fits for the majority, we have decided to model the multipath fading with Rician distribution as a basis for comparing different use cases and rooms.
It has been reported in [26] that multipath fading for the scenario where the person is moving continuously was best described by the Nakagami distribution, whereas the "walking on spot" scenario, U2, followed a Rician distribution. In our measurement the Nakagami distribution is the best fit only for the NLOS condition for U3 in room 2 and anechoic chamber. Results from room 1 show Rician distribution the best for both LOS and NLOS conditions. Another similar observation as in the literature was that the Rayleigh distribution was not the best fit for the multipath fading in the measurement rooms. It was only observed as the best fit for two NLOS conditions in

the anechoic chamber.

The estimated Rician K-factor for different body orientations and Tx - Rx separation distance is given in Table 8. The effect of body orientation on the K-factor is clearly observed in all rooms, especially in the anechoic chamber where a maximum of 19 dB difference is observed between LOS and NLOS conditions. In the conditions where the LOS path is partially or totally blocked by the body, the dominant component diminishes and the K-factor decreases. In general, a decrease in the K-factor was observed as the channel condition changed from LOS to QLOS and NLOS.

As compared to the body rotation, the effect of the body movement on the K-factor was not that significant. A maximum of 2 dB difference has been observed between static and dynamic use cases. However, it is difficult to make generalizations whether it is increased or decreased by the body movement as similar trends have not been observed for all use cases. For example, when comparing U1 and U2 the K-factor has been observed to increase with the body movement, whereas in U3 the K-factor was smaller than both U1 and U2.

The other parameter which has showed impacts on the K-factor is Tx-Rx separation. In general, for LOS conditions the K-factor was observed to decrease with increase of distance. This mainly resulted as the LOS component decays faster with increase of distance than other MPCs in the rooms, thus causing a decrease in the K-factor.

We finally discuss the influence of the room size on the K-factor. Figure 14 shows the room size dependence of K-factor for LOS condition. It has been seen that as the room size decreases, the K-factor also decreases implying higher power of multipath components contributing significantly to the received power in smaller rooms. This can be related to the theory of room electromagnetics [6] where the electromagnetic reverberation time is shown to depend only on room volume and absorption area. The results from our measurements where the antenna was not attached to the body also follow the same trend as with the LOS conditions. The finding is consistent with those of [40, 41]. The room size dependence was not very clear for the QLOS and NLOS conditions as shown in Figure 15. However, similar pattern of decreasing K-factor with smaller room size is observed for the QLOS conditions. Most probably

this is because the body is not fully blocking the LOS path and there is still some dominant component which behaves in a similar manner to the LOS conditions. Finally it is worth mentioning that similar K-factor values of U2 in Room 2 have been reported in [26]. Since the size of the room where their measurement was performed is larger than Room 1 and smaller than Room 2, this supports the observation of K-factor dependency on the room size.

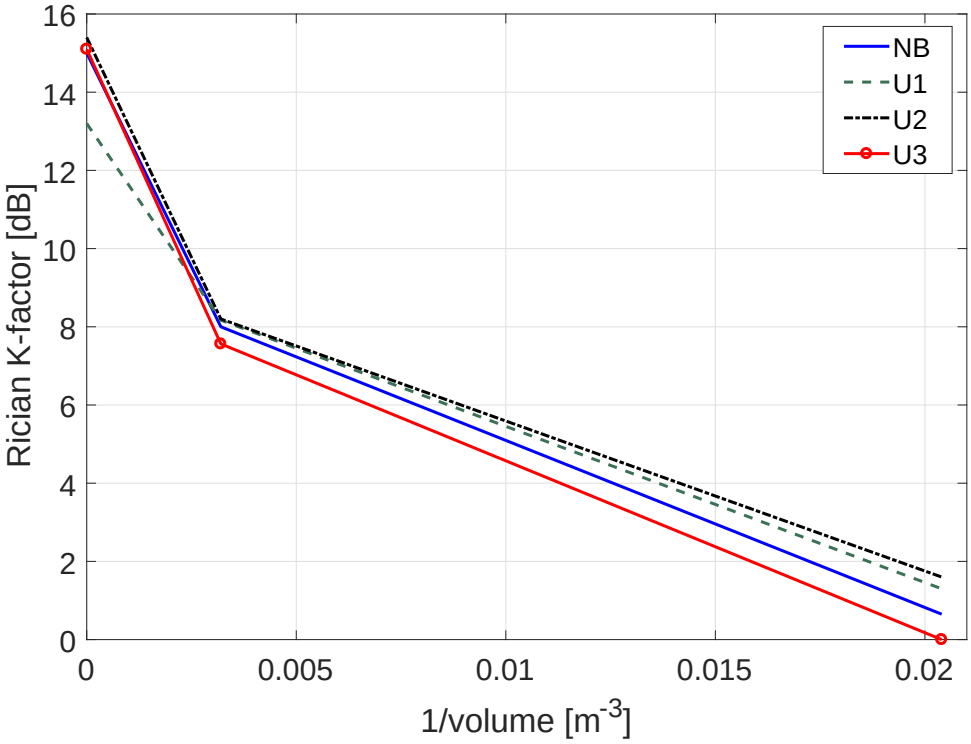


Figure 14: Rician K-factor comparison for several use cases including no-body scenario, over inverse of room volume in LOS condition

### 4.1.4 Temporal correlation

The correlation of the Gaussian components of the Rician channel has been analyzed both for the frequency and time. In addition the coherence bandwidth has been analyzed for the instantaneous channel transfer function, prior to the Gaussian component extraction, as well. The estimated coherence bandwidth, for all the measurement runs, is given in the appendix Table 23. The coherence bandwidth

Table 8: Estimates of the Rician K-factor in each measurement run

| Use case | Environment | Rotation | $k_r$[dB] | | | |
|---|---|---|---|---|---|---|
| | | | 1m | 2m | 3m | 4m |
| NB | Room 1 | LOS | −1.94 | −0.32 | 2.59 | 0.00 |
| | Room 2 | | 13.28 | 5.95 | 5.20 | 7.83 |
| | Anechoic chamber | | 17.45 | 14.49 | 13.80 | 14.56 |
| U1 | Room 1 | LOS | 4.34 | −1.39 | 0.76 | −1.09 |
| | | QLOS | −1.85 | −1.06 | 0.00 | −2.81 |
| | | NLOS | 2.91 | −0.04 | −0.72 | −1.32 |
| | Room 2 | LOS | 11.63 | 7.65 | 7.44 | 6.00 |
| | | QLOS | 7.38 | 3.73 | −3.20 | −0.96 |
| | | NLOS | 2.85 | 1.23 | −1.99 | −2.93 |
| | Anechoic chamber | LOS | 17.09 | 14.23 | 12.63 | 8.83 |
| | | QLOS | −0.51 | −2.51 | −2.70 | −2.12 |
| | | NLOS | −1.98 | −2.70 | −3.19 | −3.00 |
| U2 | Room 1 | LOS | 5.09 | 0.76 | −0.43 | −0.39 |
| | | QLOS | −0.82 | −0.13 | −1.05 | −0.95 |
| | | NLOS | −0.96 | 0.22 | −1.30 | −0.38 |
| | Room 2 | LOS | 11.84 | 9.30 | 6.21 | 5.56 |
| | | QLOS | 9.82 | 0.45 | 2.38 | 3.27 |
| | | NLOS | −1.01 | −0.94 | −2.25 | −1.19 |
| | Anechoic chamber | LOS | 19.13 | 14.75 | 13.74 | 14.25 |
| | | QLOS | 11.17 | 9.29 | 9.70 | 11.44 |
| | | NLOS | −0.30 | 0.09 | −0.55 | 0.07 |
| U3 | Room 1 | LOS | −0.89 | | | |
| | | QLOS | −1.16 | | | |
| | Room 2 | LOS | 7.69 | | | |
| | | QLOS | 0.13 | | | |
| | Anechoic chamber | LOS | 15.10 | | | |
| | | QLOS | 7.37 | | | |
| U5 | Room 3 | LOS | 9.43 | - | | |
| | | QLOS | 1.87 | - | | |
| U4 | | NLOS | 0.84 | - | | |

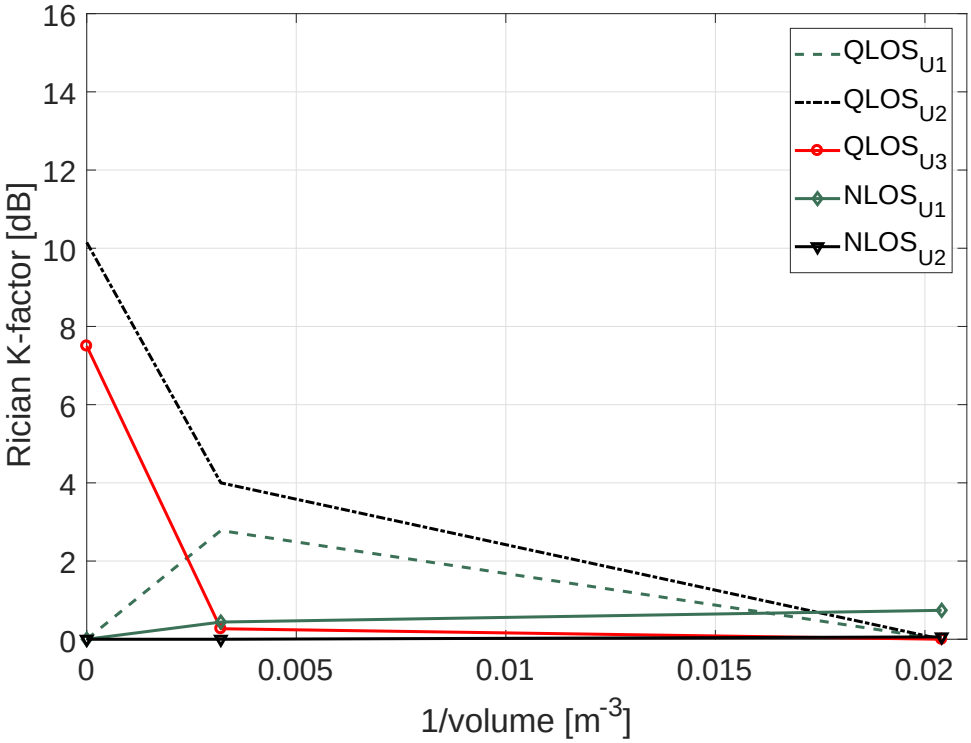


Figure 15: Rician K-factor comparison for several use cases, over inverse of room volume in QLOS and NLOS conditions

of the Gaussian components, showed variation in the range of 4 to 30 MHz for the various use cases in different measurement rooms. The overall result of the frequency correlation analysis shows higher value of coherence bandwidth for anechoic chamber as compared to Rooms 1, 2, and 3. This is expected as frequency selective fading is not observed in anechoic chamber. The body rotation has showed some effect on the coherence bandwidth, where higher values were observed during the LOS conditions. Similar range of coherence bandwidth was observed during the NB case. The body movement was not seen to affect the coherence bandwidth in Rooms 1 and 2, but it has increased the coherence bandwidth to about 10 MHz for QLOS and NLOS conditions in the anechoic chamber.

The coherence time of the Gaussian components for U2 and U3 is presented in Table 9. The results of only U2 and U3 are presented because the channel response did not vary significantly in the other static use cases. For LOS conditions at 1 meter

distance, the results show a coherence time as high as 8 seconds in anechoic chamber and Room 2. For the other use cases and channel conditions, a coherence time ranging from 0.12 to 0.64 seconds has been observed. The coherence time for LOS condition has been seen to be longer than for NLOS condition in all the results. In addition, a longer coherence time has been observed in larger rooms for LOS condition.

Table 9: Coherence time, $t_{coh}$ of the Gaussian components for U2 and U3

| Use case | Environment | Rotation | $t_{coh}$[s] | | | |
|---|---|---|---|---|---|---|
| | | | 1 m | 2 m | 3 m | 4 m |
| U2 | Room 1 | 0° | 0.16 | 0.20 | 0.16 | 0.20 |
| | | 90° | 0.16 | 0.20 | 0.16 | 0.20 |
| | | 180° | 0.16 | 0.20 | 0.16 | 0.16 |
| | | 270° | 0.20 | 0.20 | 0.24 | 0.12 |
| | Room 2 | 0° | 0.52 | 0.48 | 5.01 | 0.56 |
| | | 90° | 0.32 | 0.32 | 0.36 | 0.24 |
| | | 180° | 0.28 | 0.32 | 0.32 | 0.28 |
| | | 270° | 7.96 | 0.24 | 0.40 | 0.56 |
| | Anechoic chamber | 0° | 7.96 | 0.32 | 0.28 | 6.73 |
| | | 90° | 0.12 | 0.24 | 0.16 | 0.12 |
| | | 180° | 0.16 | 0.16 | 0.20 | 0.16 |
| | | 270° | 7.96 | 1.03 | 1.07 | 0.24 |
| U3 | Room 1 | 0° | 0.24 | | | |
| | | 180° | 0.16 | | | |
| | Room 2 | 0° | 0.60 | | | |
| | | 180° | 0.24 | | | |
| | Anechoic chamber | 0° | 0.64 | | | |
| | | 180° | 0.16 | | | |

### 4.1.5 Delay spread

Delay spread estimates of all measurements are presented in the appendix Tables 24 - 26. The RMS delay spread is expected to be very small in the anechoic chamber and the results support this for the LOS conditions. However, body rotation has resulted in an increase in the RMS delay spread as the diffracted waves around the body were contributing to the received power in QLOS and NLOS conditions. The difference caused by the body rotation was higher in the measurement rooms. It was also found that a smaller room shows greater RMS delay spread than 15 ns. Although not significant as body rotation, movement has also resulted in an increased delay spread. The effect of Tx - Rx separation distance has been clearly noticed in the NB and LOS conditions, where the RMS delay spread is longer with distance. Generally, the measured RMS delay spread in all measurement environments was in the range of 4 to 30 ns. The typical MBAN channel has a symbol rate of 1 or 2 M symbol/s, with a corresponding symbol length of 0.5 or 1 $\mu$s. Therefore the MBAN channel can be considered as a narrowband channel since the measured RMS delay spread is much lower than the symbol length.

## 4.2 Improved channel model

The final step of the thesis work is to reproduce realistic time-varying radio channel transfer functions of each use case based on the analyzed properties of the channels, i.e., path loss, shadow fading, Rician K-factor and fading correlation. This follows the same step done in the analysis phase in a reverse order, whereby we first generate the three model components independently and then add them up to have the instantaneous channel transfer functions based on the given input parameters such as the room size, body posture, and Tx - Rx separation distance.

### 4.2.1 Model implementation

Table 10 describes the main parameters and options of the model. These are: room size, Tx - Rx separation distance, user action, and rotation. The room size is notified

Table 10: Model input parameters

| **Body action (P1)** | **Orientation (P2)** | **Room size (P3)** | **Distance (P4)** |
|---|---|---|---|
| Lie down | LOS | Range 1 | |
| Stand | QLOS | Range 2 | 1-4 m |
| Walk | NLOS | Range 3 | |

Table 11: Model dependency

| **Input Parameters** | **Dependent components** | |
|---|---|---|
| P1 | Body shadowing<br>$\mu$, $\sigma$ | Coherence time<br>$t_{coh}$ |
| P2 | All | |
| P3 | Path loss exponent<br>$n$ | Multipath fading<br>$K_r$ |
| P4 | Multipath fading<br>$K_r$ | |

in three ranges where rooms with comparable volume to the measurement Room 1 are categorized in Range 1, rooms with comparable volume to the measurement Room 2 are categorized in Range 2, and rooms with much larger volume than the measurement Room 2 are categorized in Range 3. The path loss exponent, reference path loss, shadowing lognormal parameters, Rician K-factor, and coherence values are chosen based on these input parameters. The components which are dependent on the input model parameters are shown in Table 11. The mean path loss is calculated based on the link distance, room size, and body orientation. The body shadowing is generated from the lognormal distribution based on body movement. The multipath component is generated based on the room size, Tx - Rx separation distance, and body orientation.

Depending on the body action, two methods have been followed to reproduce the channel transfer functions. For static use cases, such as U1, U4, and U5 the multipath

component has been generated as a function of frequency as

$$\boldsymbol{h}(f) = \sqrt{\frac{K_r}{K_r+1}}\exp(-\mathrm{j}2\pi \boldsymbol{f}\tau_{\mathrm{LOS}}) + \sqrt{\frac{1}{K_r+1}}\boldsymbol{h}_{\mathrm{iid}}\boldsymbol{\rho}_f^{\frac{1}{2}}, \tag{28}$$

where $\tau_{\mathrm{LOS}} = \frac{d_{\mathrm{LOS}}}{c}$ is the delay of the LOS, $\boldsymbol{h}_{\mathrm{iid}} \sim \mathcal{CN}(\mu, \sigma^2)$ is a vector of complex identical independently distributed (iid) Gaussian random variables, and $\boldsymbol{\rho}_f$ is the frequency correlation matrix. Then the total instantaneous path loss follows from (19) as

$$L_{PT}(f)_{[\mathrm{dB}]} = \overline{L_P}_{[\mathrm{dB}]} + \Delta L_{B[\mathrm{dB}]} + \Delta L_F(f)_{[\mathrm{dB}]}, \tag{29}$$

where $\Delta L_F(f)_{[\mathrm{dB}]} = 10\log_{10}(|h(f)|^2)$.

For the dynamic use cases, such as U2 and U3, the multipath component has been generated as a function of frequency and time as

$$\boldsymbol{H}(f,t) = \sqrt{\frac{K_r}{K_r+1}}\exp(-\mathrm{j}2\pi \boldsymbol{f}\tau_{\mathrm{LOS}}) + \sqrt{\frac{1}{K_r+1}}\boldsymbol{\rho}_t^{\frac{1}{2}}\boldsymbol{H}_{\mathrm{iid}}\boldsymbol{\rho}_f^{\frac{1}{2}}, \tag{30}$$

where in this case $\boldsymbol{H}_{\mathrm{iid}} \sim \mathcal{CN}(\mu, \sigma^2)$ is a matrix of complex iid Gaussian random variables, and $\boldsymbol{\rho}_t$ is the time correlation matrix. The total instantaneous path loss becomes

$$L_{PT}(f,t)_{[\mathrm{dB}]} = \overline{L_P}_{[\mathrm{dB}]} + \Delta L_{B[\mathrm{dB}]} + \Delta L_F(f,t)_{[\mathrm{dB}]}, \tag{31}$$

where $\Delta L_F(f,t)_{[\mathrm{dB}]} = 10\log_{10}(|h(f,t)|^2)$.

The frequency and time correlation matrices have been calculated from the coherence bandwidth and time by using the Bessel function as

$$\boldsymbol{\rho}_f = \mathrm{toeplitz}\left(J_0\left(\Delta f \frac{1.52}{B_{coh}}\right)\right), \tag{32}$$

$$\boldsymbol{\rho}_t = \mathrm{toeplitz}\left(J_0\left(\Delta t \frac{1.52}{t_{coh}}\right)\right), \tag{33}$$

where toeplitz is a Matlab function which constructs a Toeplitz matrix, and $J_0$ is the Bessel function of the zeroth order.

### 4.2.2 Model validation

Finally, the improved model has been validated by comparing the empirical and reproduced CDFs of the channel gain. The comparison presented in Figure 16 is for the continuous movement use case, U3, whereas the comparison at discrete Tx - Rx distances in the use cases U1 and U2 are given in the appendix Figures 18 - 25. In addition, the comparison for the use cases U4 and U5 are shown in Figure 17. In general, it has been observed that for the majority of the use cases the correlation between reproduced and measured channel gain is always greater than 0.95.

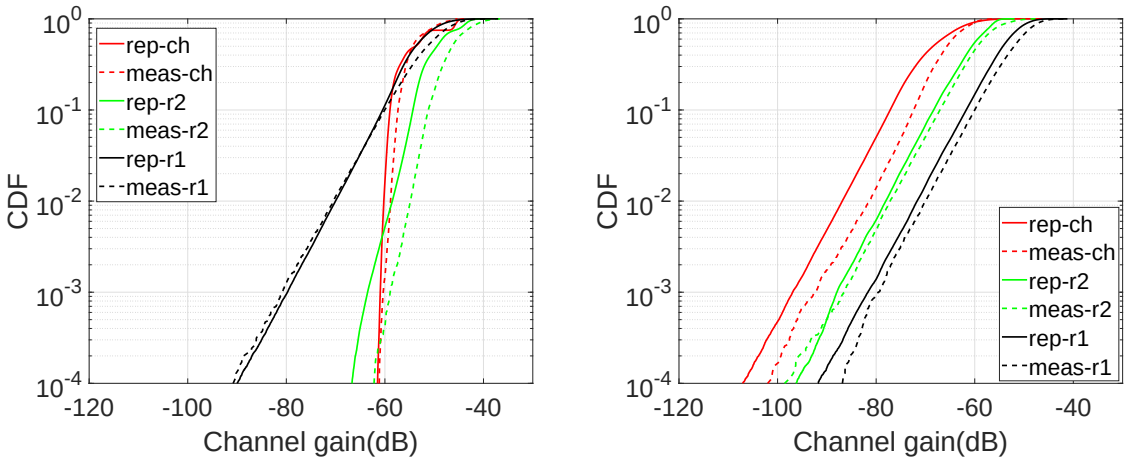


(a) LOS (b) QLOS

Figure 16: Comparison of the reproduced and measured channel gain for U3, in Room 1, Room 2, and Anechoic chamber

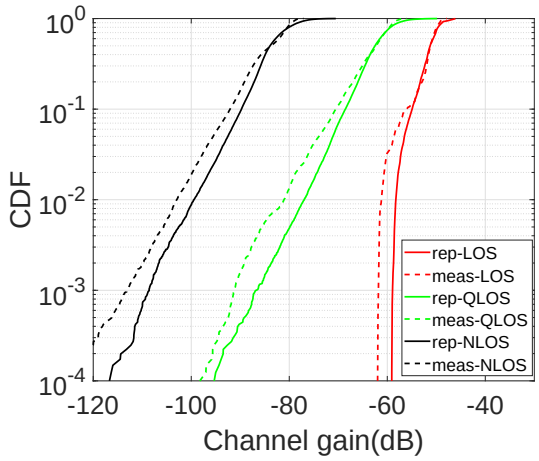


Figure 17: Comparison of the reproduced and measured channel gain for U4 and U5, at various channel conditions

# 5 Summary and Conclusion

The application of wireless technology in patient monitoring increases the demand for accurate characterization of the MBAN propagation channel. A methodology for testing an MBAN device performance has been developed in this thesis. This methodology implements an improved channel model for the MBAN device based on user scenario and room size dependency. Therefore, it answers the research questions on the optimal way to reflect the effect of patient movement, posture, rotation, and room size on the MBAN channel.

This methodology has been developed in three main phases: the measurement, modeling, and implementation phase. Considering the dynamic nature of the patient and different interaction with the surrounding environment in the hospital room, a stochastic model was chosen to properly characterize the MBAN channel. The frequency range of the measurement was from 2.3 GHz to 2.5 GHz covering the MBAN and ISM bands. The measurement was planned based on the research questions to study different device use scenarios and room size dependency of the MBAN channel. The use cases were defined by considering the most possible uses of the MBAN device. Thus the patient posture, upright position or lying in bed, was the first parameter in defining the use cases. The second parameter was body movement, where both on spot and continuous walking movement were considered. In addition, these measurements were carried out in three office rooms of different sizes and an anechoic chamber to further study the impact of the room size on the MBAN channel.

The measured channel transfer functions for the different use cases and environments differ significantly. Body rotation, which indicates whether the channel is LOS, QLOS, or NLOS conditions, has the highest impact on the link, where $>$ 30dB attenuation of received power is observed in NLOS conditions as compared to LOS conditions. In addition, body movement has resulted in about 3dB fluctuation of the received power, which is very minor as compared to the impact of body rotation. Furthermore, the impact of room size on the measured channel has been clear in

LOS conditions where small rooms experience a larger amount of deep fades than large rooms. Whereas, in NLOS conditions the frequency of observing deep fades in the channel is similar regardless of the room size but the mean received power is smaller in larger rooms. During the worst case scenario of the lying down position, U4 90° rotation, where the sensor antenna was sandwiched between the hip and the bed, the probability that the channel gain was above the threshold value of −90dB was only 10%.

The analysis of the measurement data and modeling part followed the general method of characterizing the channel in three main components: the mean path loss, the body shadowing, and the multipath fading. The mean path loss component was modeled so that it monotonically decreases as a distance log function, while the body shadowing was modeled by a lognormal distribution, and the multipath fading component was modeled by a Rician distribution. The complete channel model was then constructed by combining these model parameters for the different use cases and a size of rooms. The model was implemented by using the use cases, channel conditions, and room size as input parameters to produce realistic channel response. The model successfully reproduces frequency and time correlation of the measured channel response. The proposed model has been validated by comparing its channel gain statistics with measurements.

The proposed channel model offers flexibility on changing the room size, as hospital room size is expected to vary considerably. This feature is not found in existing BAN channel models such as [4], and [26]. In addition, the model is novel as it characterizes the wideband channel from 2.3 GHz to 2.5 GHz. Furthermore, the model allows us to analyze the effects of each influencing factor on radio channels, for example, body movement or rotation, separately. The parameter values of path loss exponent, body shadowing, and multipath fading are adjustable based on the use cases, channel conditions, location of patient in the room, and the room size. In general, the developed methodology can be used in MBAN device testing for performance validation or improvement.

The accuracy of the methodology is affected by the limitations of the measurement

equipment including their setup, rigorousness of the post processing and modeling. Since the model was developed based on measurements, the most obvious inaccuracies of the model result from channel sounding and post-processing errors based on various assumptions. The assumption of no correlation between body shadowing and multipath fading has been seen not always valid because of the influence of body movement in the multipath fading parameter; the Rician K-factor. The other assumption of the methodology is in room size dependency; as measurements were performed in rooms with different furniture that had a significant effect on the MBAN channel, and the volume of the room was calculated as if it was empty. This implies that the reported K-factor values might be smaller if compared with results from empty room of the same volume.

As the RMS delay spreads in most use cases were shorter than the symbol length, it is recommended to emulate the developed channel model with simple amplifier/attenuator for an over-the-air MBAN channel testing. The frequency correlation analysis in the developed methodology can be utilized in developing diversity mechanisms, such as frequency hopping. Possible future works include, further study on the correlation of body shadowing and multipath fading, coexistence of multiple MBAN devices, and MBAN on-body communication links. The proposed model does not consider blockage by other objects other than the human body where the sensor is attached, or even a second human blockage, for example, by a physician or nurse treating the patient. This blockage can be further included in this model to increase its accuracy at the expense of increased complexity. Additional study could be made on multipath fading which results from moving objects in the room, such as other patients or visitors moving in the room.

# References

[1] IEEE Standard for Local and Metropolitan Area Networks Part 15.6: Wireless Body Area Networks, IEEE Std. 802.15.6-2012, Feb. 2012.

[2] FCC - Medical Body Area Networks - small entity compliance guide. [Online]. Available: `http://www.fcc.gov/document/medical-body-area-networks`

[3] IEEE Standard for Local and metropolitan area networks Part 15.4: Low-Rate Wireless Personal Area Networks (LR-WPANs), Amendment 4: Alternative Physical Layer Extension to Support Medical Body Area Network (MBAN) Services Operating in the 2360 to 2400 MHz Band, Tech. Rep. IEEE Std 802.15.4j, February, 2013.

[4] K. Y. Yazdandoost and K. Sayrafian-Pour, "Channel model for body area network," Tech. Rep. IEEE P802.15-08-0780-09-0006, Apr. 2009.

[5] M. Mackowiak and L. M. Correia, "Statistical path loss model for dynamic off-body channels," in *Proc. 2014 IEEE 25th Annual International Symposium on Personal, Indoor, and Mobile Radio Communication (PIMRC)*, Washington DC, USA, Sep. 2014, pp. 53-57.

[6] J. Bach Andersen, J. Ø. Nielsen, G. F. Pedersen, G. Bauch, and M. Herdin. "Room electromagnetics," *IEEE Ant. Prop. Mag.*, vol. 49, no. 2, pp. 27-33, Apr. 2007.

[7] D. M. Davenport, B. Deb and F. J. Ross, "Wireless propagation and coexistence of medical body sensor networks for ambulatory patient monitoring," in *Proc. 2009 Sixth International Workshop on Wearable and Implantable Body Sensor Networks*, Berkeley, CA, USA, June 2009, pp. 41-45.

[8] B. Godara, K. S Nikita, *Wireless Mobile Communication and Healthcare*, Springer, 2013.

[9] S. R. Saunders and A. Aragon-Zavala, *Antennas and Propagation for Wireless Communication Systems*, 2nd edition, Wiley, 2007.

[10] A. F. Molisch, *Wireless Communications*, IEEE Press, 2005.

[11] T. S. Rappaport, *Wireless Communication: Principles and Practice*, 2nd edition: Prentice Hall, 2002.

[12] P. S. Hall, *Antennas and Propagation for Body-Centric Wireless Communications*, Second Edition, Artech House, 2012.

[13] J. Wang, Q. Wang, *Body Area Communications: Channel Modeling, Communication Systems, and EMC*, John Wiley & Sons, 2012.

[14] J. Kunisch and J. Pamp, "Ultra-wideband double vertical knife-edge model for obstruction of a ray by a person," in *Proc. 2008 IEEE International Conference on Ultra-Wideband*, Hannover, Germany, Sep. 2008, pp. 17-20.

[15] M. Mackowiak, C. Oliveira, C. Lopes and L. M. Correia, "A statistical analysis of the influence of the human body on the radiation pattern of wearable antennas," in *Proc. 2011 IEEE 22nd International Symposium on Personal, Indoor and Mobile Radio Communications*, Toronto, Canada, Sep. 2011, pp. 2214-2218.

[16] L. Ahlin, J. Zander, B. Slimane, *Principles of Wireless Communications*, Studentlitteratur, 2006.

[17] H. H. Xia, H. L. Bertoni, L. R. Maciel, A. Lindsay-Stewart and R. Rowe, "Microcellular propagation characteristics for personal communications in urban and suburban environments," *IEEE Trans. Veh. Tech.*, vol. 43, no. 3, pp. 743-752, Aug. 1994.

[18] P. F. Cui, Y. Yu, W. J. Lu, Y. Liu and H. B. Zhu, "Measurement and modeling of wireless off-body propagation characteristics under hospital environment at 6-8.5 GHz," *IEEE Access*, vol. 5, pp. 10915-10923, May 2017.

[19] H. Bertoni, *Radio Propagation for Modern Wireless Systems*, Prentice Hall, 2000.

[20] S. S. Haykin, M. Moher, *Modern Wireless Communications*, Pearson Prentice Hall, 2005.

[21] M. K. Simon and M.-S. Alouini, *Digital Communications over Fading Channels*, Wiley Series in Telecommunications and Signal Processing, 2nd ed., 2004.

[22] J. Poutanen, K. Haneda, J. Salmi, V-M. Kolmonen, A. Richter, P. Almers, and P. Vainikainen, "Development of measurement-based ray tracer for multi-link double directional propagation parameters," in *Proc. 3rd European Conference on Antennas and Propagation 2009 (EuCAP 2009)*, Berlin, Germany, Mar. 2009, pp. 2622-2626.

[23] A. Goldsmith, *Wireless Communications*, Cambridge, Cambridge Univ. Press, 2005.

[24] K. S. Kunz, R. J. Luebbers, *The Finite Difference Time Domain Method for Electromagnetics*, CRC Press, 1993.

[25] R. Harrington, *Field Computation by Moment Methods*, Wiley-IEEE Press, 1993.

[26] S. J. Ambroziak, L. M. Correia, R. J. Katulski, M. Mackowiak, C. Oliveira, J. Sadowski and K. Turbic, "An off-body channel model for body area networks in indoor environments," *IEEE Trans. Ant. Prop.*, vol. 64, no. 9, pp. 4022-4035, Sep. 2016.

[27] S. L. Cotton, R. D'Errico, C. Oesteges, "A Review of radio channel models for body centric communications," *Radio Sci.*, vol. 49, no. 6, pp. 371-388, June 2014.

[28] R. Cavallari, F. Martelli, R. Rosini, C. Buratti, and R. Verdone, "A survey on wireless body area networks: Technologies and design challenges," *IEEE Commun. Surveys Tuts.*, vol. 16, no. 3, pp. 1635-1657, Feb. 2014.

[29] M. Mohamed, M. Cheffena, A. Moldsvor and F. P. Fontan, "Physical-statistical channel model for off-body area network," *IEEE Ant. Wireless Prop. Lett.*, vol. 16, pp. 1516-1519, Jan. 2017.

[30] G. Roqueta, A. Fort, C. Craeye and C. Oestges, "Analytical propagation models for body area networks," in *Proc. 2007 IET Seminar on Antennas and Propagation for Body-Centric Wireless Communications*, London, UK, Apr. 2007, pp. 90-96.

[31] O. P. Pasquero, R. D'Errico, M. Mhedhbi, B. Uguen, CORMORAN Deliverable D2.2 - 1st Channel measurement campaign and identification of relevant radio models and parameters. [Online]. Available: `http://pylayers.github.io/pylayers/cormoran.html`

[32] D. Miniutti, L. Hanlen, D. Smith, A. Zhang, D. Lewis, D. Rodda, B. Gilbert, "Narrowband on body to off body channel characterization for BAN," Tech. Rep. IEEE 802.15-08-0559-00-0006, Aug. 2008.

[33] H. Sawada, T. Aoyagi, J. Takada, K. Y. Yazdandoost, R. Kohno, "Channel model between body surface and wireless access point for UWB band," Tech. Rep. IEEE 802.15-08-0576-00-0006, Aug. 2008.

[34] MATLAB. MathWorks Inc. Natick, Massachusetts, USA. [Online]. Available: `https://se.mathworks.com/products/matlab.html`

[35] R. A. Valenzuela, O. Landron, and D. L. Jacobs, "Estimating local mean signal strength of indoor multipath propagation," *IEEE Trans. Veh. Tech.*, vol. 46, no. 1, pp. 203-212, Feb. 1997.

[36] M. H. DeGroot and M. J. Schervish, *Probability and Statistics*, Pearson, 4th ed., 2011.

[37] L. J. Greenstein, D. G. Michelson and V. Erceg, "Moment-method estimation of the Ricean K-factor," *IEEE Commun. Lett.*, vol. 3, no. 6, pp. 175-176, June 1999.

[38] R. Rosini and R. D'Errico, "Off-body channel modelling at 2.45 GHz for two different antennas," in *Proc. 6th European Conference on Antennas and Propagation (EUCAP, 2012)*, Prague, Czech Republic, Mar. 2012, pp. 3378-3382.

[39] S. J. Ambroziak, L. M. Correia, R. J. Katulski, and M. Mackowiak, "Measurements of path loss in off-body channels in indoor environments," in *Proc. 1st URSI Atlantic Radio Science Conference (URSI AT-RASC)*, Gran Canaria, Spain, May 2015, p. 1.

[40] Y. Lustmann, D. Porrat, "Indoor channel spectral statistics, K-factor and reverberation distance," *IEEE Trans. Ant. Prop.*, vol. 58, no. 11, pp. 3685-3692, Nov. 2010.

[41] R. A. Valenzuela, D. Chizhik, J. Ling, "Measured and predicted correlation between local average power and small scale fading in indoor wireless communication channels," in *Proc. IEEE 48th Vehicular Technology Conference*, vol. 3, May 1998, pp. 2104-2108.

# A Appendix

This appendix contains the post-processed measurement results, model parameters and model validations.

## A.1 Mean path loss

Table 12: Measured mean path loss for several use cases in Anechoic chamber

| Use case | Rotation | $L_{p[dB]}$ | | | |
|---|---|---|---|---|---|
| | | 1m | 2m | 3m | 4m |
| U1 | 0° | 50 | 53 | 54 | 57 |
| | 90° | 72 | 72 | 73 | 72 |
| | 180° | 64 | 66 | 69 | 70 |
| | 270° | 41 | 49 | 53 | 56 |
| U2 | 0° | 45 | 53 | 56 | 58 |
| | 90° | 76 | 75 | 77 | 76 |
| | 180° | 60 | 59 | 62 | 62 |
| | 270° | 41 | 48 | 51 | 54 |
| NB | 0° | 36 | 42 | 46 | 49 |

Table 13: Measured mean path loss for several use cases in Room 1

| Use case | Rotation | $L_{p[dB]}$ | | | |
|---|---|---|---|---|---|
| | | 1m | 2m | 3m | 4m |
| U1 | 0° | 43 | 49 | 51 | 52 |
| | 90° | 51 | 54 | 54 | 52 |
| | 180° | 51 | 55 | 54 | 53 |
| | 270° | 42 | 48 | 50 | 49 |
| U2 | 0° | 48 | 52 | 53 | 53 |
| | 90° | 56 | 56 | 55 | 56 |
| | 180° | 51 | 54 | 54 | 55 |
| | 270° | 40 | 48 | 50 | 53 |
| NB | 0° | 37 | 41 | 41 | 44 |

Table 14: Measured mean path loss for several use cases in Room 2

| Use case | Rotation | $L_{p[dB]}$ | | | |
|---|---|---|---|---|---|
| | | 1m | 2m | 3m | 4m |
| U1 | 0° | 40 | 46 | 49 | 52 |
| | 90° | 56 | 60 | 62 | 63 |
| | 180° | 48 | 51 | 57 | 58 |
| | 270° | 37 | 43 | 46 | 49 |
| U2 | 0° | 43 | 48 | 50 | 52 |
| | 90° | 59 | 61 | 61 | 65 |
| | 180° | 43 | 50 | 53 | 57 |
| | 270° | 33 | 40 | 46 | 53 |
| NB | 0° | 37 | 42 | 46 | 49 |

Table 15: Measured mean path loss at 1m distance, for U4 and U5

| Use case | Rotation | $L_{p[dB]}$ |
|---|---|---|
| U4 | 0° | 59 |
| | 90° | 80 |
| U5 | 0° | 48 |
| | 90° | 50 |

## A.2 Body shadowing model parameters

Table 16: Body shadowing lognormal model parameters for several use cases in an anechoic chamber

| Use case | Rotation | Distance [m] | $\mu_{[\mathrm{dB}]}$ | $\sigma_{[\mathrm{dB}]}$ |
|---|---|---|---|---|
| U1 | 0° | 1 | 0.00 | 0.06 |
| | | 2 | 0.00 | 0.08 |
| | | 3 | 0.00 | 0.99 |
| | | 4 | 0.00 | 0.15 |
| | 90° | 1 | 0.00 | 0.31 |
| | | 2 | 0.00 | 0.30 |
| | | 3 | 0.00 | 0.31 |
| | | 4 | 0.00 | 0.29 |
| | 180° | 1 | 0.00 | 0.17 |
| | | 2 | 0.00 | 0.18 |
| | | 3 | 0.00 | 0.28 |
| | | 4 | 0.00 | 0.28 |
| | 270° | 1 | 0.00 | 0.05 |
| | | 2 | 0.00 | 0.05 |
| | | 3 | 0.00 | 0.08 |
| | | 4 | 0.00 | 0.09 |
| U2 | 0° | 1 | 0.00 | 0.17 |
| | | 2 | 0.00 | 0.37 |
| | | 3 | 0.00 | 0.45 |
| | | 4 | 0.00 | 0.48 |
| | 90° | 1 | 0.00 | 2.14 |
| | | 2 | 0.00 | 1.19 |
| | | 3 | 0.00 | 1.01 |
| | | 4 | 0.00 | 1.48 |
| | 180° | 1 | 0.00 | 0.80 |
| | | 2 | 0.00 | 0.97 |
| | | 3 | 0.00 | 0.88 |
| | | 4 | 0.00 | 0.71 |
| | 270° | 1 | 0.00 | 0.31 |
| | | 2 | 0.00 | 0.44 |
| | | 3 | 0.00 | 0.29 |
| | | 4 | 0.00 | 0.33 |
| U3 | 0° | 1 - 4 | −0.13 | 1.06 |
| | 180° | | −0.09 | 0.88 |

Table 17: Body shadowing lognormal model parameters for several use cases in Room 1

| Use case | Rotation | Distance [m] | $\mu_{[\mathrm{dB}]}$ | $\sigma_{[\mathrm{dB}]}$ |
|---|---|---|---|---|
| U1 | 0° | 1 | 0.00 | 0.04 |
| | | 2 | −0.01 | 0.25 |
| | | 3 | −0.01 | 0.36 |
| | | 4 | −0.11 | 0.99 |
| | 90° | 1 | −0.01 | 0.31 |
| | | 2 | −0.03 | 0.50 |
| | | 3 | −0.02 | 0.39 |
| | | 4 | −0.01 | 0.32 |
| | 180° | 1 | 0.00 | 0.09 |
| | | 2 | −0.02 | 0.40 |
| | | 3 | 0.00 | 0.14 |
| | | 4 | −0.01 | 0.35 |
| | 270° | 1 | 0.00 | 0.10 |
| | | 2 | 0.00 | 0.08 |
| | | 3 | −0.01 | 0.27 |
| | | 4 | −0.06 | 0.74 |
| U2 | 0° | 1 | −0.04 | 0.57 |
| | | 2 | −0.07 | 0.79 |
| | | 3 | −0.12 | 1.02 |
| | | 4 | −0.04 | 0.60 |
| | 90° | 1 | −0.06 | 0.74 |
| | | 2 | −0.07 | 0.80 |
| | | 3 | −0.15 | 1.19 |
| | | 4 | −0.21 | 1.25 |
| | 180° | 1 | −0.09 | 0.88 |
| | | 2 | −0.03 | 0.53 |
| | | 3 | −0.03 | 0.49 |
| | | 4 | −0.15 | 1.15 |
| | 270° | 1 | −0.04 | 0.59 |
| | | 2 | −0.04 | 0.56 |
| | | 3 | −0.03 | 0.52 |
| | | 4 | −0.21 | 1.34 |
| U3 | 0° | 1 - 4 | −0.22 | 1.37 |
| | 180° | | −0.14 | 1.11 |

Table 18: Body shadowing lognormal model parameters for several use cases in Room2

| Use case | Rotation | Distance [m] | $\mu_{[\mathrm{dB}]}$ | $\sigma_{[\mathrm{dB}]}$ |
|---|---|---|---|---|
| U1 | 0° | 1 | 0.00 | 0.04 |
| | | 2 | 0.00 | 0.03 |
| | | 3 | 0.00 | 0.05 |
| | | 4 | −0.01 | 0.21 |
| | 90° | 1 | −0.07 | 0.78 |
| | | 2 | 0.00 | 0.15 |
| | | 3 | 0.00 | 0.15 |
| | | 4 | −0.01 | 0.24 |
| | 180° | 1 | 0.00 | 0.20 |
| | | 2 | −0.01 | 0.25 |
| | | 3 | 0.00 | 0.18 |
| | | 4 | 0.00 | 0.11 |
| | 270° | 1 | 0.00 | 0.03 |
| | | 2 | 0.00 | 0.07 |
| | | 3 | 0.00 | 0.06 |
| | | 4 | 0.00 | 0.06 |
| U2 | 0° | 1 | −0.01 | 0.27 |
| | | 2 | −0.01 | 0.31 |
| | | 3 | −0.02 | 0.42 |
| | | 4 | −0.08 | 0.87 |
| | 90° | 1 | −0.16 | 1.19 |
| | | 2 | −0.11 | 0.97 |
| | | 3 | −0.02 | 0.40 |
| | | 4 | −0.06 | 0.73 |
| | 180° | 1 | −0.09 | 0.87 |
| | | 2 | −0.07 | 0.77 |
| | | 3 | −0.02 | 0.45 |
| | | 4 | −0.05 | 0.65 |
| | 270° | 1 | −0.02 | 0.44 |
| | | 2 | −0.01 | 0.27 |
| | | 3 | 0.00 | 0.15 |
| | | 4 | −0.01 | 0.21 |
| U3 | 0° | 1 - 4 | −0.12 | 1.01 |
| | 180° | | −0.15 | 1.15 |

## A.3 Statistical description of multipath fading

Table 19: Multipath fading distribution best fits for use cases U4 and U5

| Use case | Rotation | Distribution | Parameters |
|---|---|---|---|
| U4 | 0° | Rician | $s = 0.8$, $\sigma = 0.4$ |
| | 90° | Normal | $\mu = 0.9, \sigma = 0.4$ |
| U5 | 0° | Weibull | $a = 1.1$, $b = 5.0$ |
| | 90° | Nakagami | $m = 1.9$, $\omega = 1.0$ |

Table 20: Multipath fading distribution best fits of all measured use cases, in anechoic chamber

| Use case | distance [m] | Rotation | Distribution | Parameters |
|---|---|---|---|---|
| U1 | 1 | 0° | Weibull | $a = 1.0$, $b = 12.0$ |
| | | 90° | Weibull | $a = 1.0$, $b = 2.0$ |
| | | 180° | Rician | $s = 0.8$, $\sigma = 0.5$ |
| | | 270° | Weibull | $a = 1.0$, $b = 12.5$ |
| | 2 | 0° | Weibull | $a = 1.0$, $b = 10.2$ |
| | | 90° | Rayleigh | $\sigma = 0.7$ |
| | | 180° | Nakagami | $m = 1.3$, $\omega = 1.0$ |
| | | 270° | Lognormal | $\mu = 0.0, \sigma = 0.1$ |
| | 3 | 0° | Lognormal | $\mu = 0.0, \sigma = 0.2$ |
| | | 90° | Rayleigh | $\sigma = 0.7$ |
| | | 180° | Rician | $s = 0.7$, $\sigma = 0.5$ |
| | | 270° | Nakagami | $m = 10.8$, $\omega = 1.0$ |
| | 4 | 0° | Weibull | $a = 1.1$, $b = 4.2$ |
| | | 90° | Rician | $s = 0.5$, $\sigma = 0.6$ |
| | | 180° | Rician | $s = 0.7$, $\sigma = 0.5$ |
| | | 270° | Weibull | $a = 1.1$, $b = 5.5$ |
| U2 | 1 | 0° | Weibull | $a = 1.0$, $b = 16.3$ |
| | | 90° | Rician | $s = 0.7$, $\sigma = 0.5$ |
| | | 180° | Weibull | $a = 1.1$, $b = 6.2$ |
| | | 270° | Weibull | $a = 1.0$, $b = 16.1$ |
| | 2 | 0° | Weibull | $a = 1.1$, $b = 8.1$ |
| | | 90° | Rician | $s = 0.6$, $\sigma = 0.6$ |
| | | 180° | Normal | $\mu = 1.0, \sigma = 0.2$ |
| | | 270° | Gamma | $a = 84.9$, $b = 0.0$ |
| | 3 | 0° | Weibull | $a = 1.0$, $b = 7.1$ |
| | | 90° | Rician | $s = 0.7$, $\sigma = 0.5$ |
| | | 180° | Normal | $\mu = 1.0, \sigma = 0.2$ |
| | | 270° | Weibull | $a = 1.1$, $b = 9.0$ |
| | 4 | 0° | Weibull | $a = 1.1$, $b = 8.1$ |
| | | 90° | Rician | $s = 0.7$, $\sigma = 0.5$ |
| | | 180° | Weibull | $a = 1.1$, $b = 6.0$ |
| | | 270° | Rician | $s = 1.0$, $\sigma = 0.1$ |
| U3 | 1-4 | 0° | Nakagami | $m = 14.9$, $\omega = 1.0$ |
| | | 180° | Rician | $s = 0.9$, $\sigma = 0.3$ |
| NB | 1 | 0° | Weibull | $a = 1.0$, $b = 12.8$ |
| | 2 | | Lognormal | $\mu = -0.0, \sigma = 0.1$ |
| | 3 | | Nakagami | $m = 13.3$, $\omega = 1.0$ |
| | 4 | | Weibull | $a = 1.1$, $b = 9.2$ |

Table 21: Multipath fading distribution best fits for all measured use cases, in Room 1

| Use case | distance [m] | Rotation | Distribution | Parameters |
|---|---|---|---|---|
| U1 | 1 | 0° | Weibull | $a = 1.1$, $b = 3.7$ |
| | | 90° | Rician | $s = 0.8$, $\sigma = 0.4$ |
| | | 180° | Rician | $s = 0.7$, $\sigma = 0.5$ |
| | | 270° | Weibull | $a = 1.0$, $b = 2.7$ |
| | 2 | 0° | Nakagami | $m = 0.7$, $\omega = 1.0$ |
| | | 90° | Rician | $s = 0.8$, $\sigma = 0.5$ |
| | | 180° | Gamma | $a = 3.3$, $b = 0.3$ |
| | | 270° | Rician | $s = 0.7$, $\sigma = 0.5$ |
| | 3 | 0° | Rician | $s = 0.7$, $\sigma = 0.5$ |
| | | 90° | Nakagami | $m = 0.8$, $\omega = 1.0$ |
| | | 180° | Gamma | $a = 2.9$, $b = 0.3$ |
| | | 270° | Rician | $s = 0.8$, $\sigma = 0.4$ |
| | 4 | 0° | Rician | $s = 0.6$, $\sigma = 0.6$ |
| | | 90° | Nakagami | $m = 1.1$, $\omega = 1.0$ |
| | | 180° | Weibull | $a = 1.0$, $b = 2.2$ |
| | | 270° | Rician | $s = 0.7$, $\sigma = 0.5$ |
| U2 | 1 | 0° | Rician | $s = 0.8$, $\sigma = 0.5$ |
| | | 90° | Rician | $s = 0.6$, $\sigma = 0.6$ |
| | | 180° | Rician | $s = 0.7$, $\sigma = 0.5$ |
| | | 270° | Rician | $s = 1.0$, $\sigma = 0.2$ |
| | 2 | 0° | Rician | $s = 0.6$, $\sigma = 0.6$ |
| | | 90° | Rician | $s = 0.8$, $\sigma = 0.5$ |
| | | 180° | Rician | $s = 0.7$, $\sigma = 0.5$ |
| | | 270° | Rician | $s = 0.9$, $\sigma = 0.4$ |
| | 3 | 0° | Rician | $s = 0.6$, $\sigma = 0.6$ |
| | | 90° | Rician | $s = 0.7$, $\sigma = 0.5$ |
| | | 180° | Rician | $s = 0.7$, $\sigma = 0.5$ |
| | | 270° | Rician | $s = 0.7$, $\sigma = 0.5$ |
| | 4 | 0° | Rician | $s = 0.7$, $\sigma = 0.5$ |
| | | 90° | Rician | $s = 0.8$, $\sigma = 0.5$ |
| | | 180° | Weibull | $a = 1.0$, $b = 2.2$ |
| | | 270° | Rician | $s = 0.7$, $\sigma = 0.5$ |
| U3 | 1-4 | 0° | Rician | $s = 0.6$, $\sigma = 0.6$ |
| | | 180° | Rician | $s = 0.7$, $\sigma = 0.5$ |
| NB | 1 | 0° | Nakagami | $m = 0.9$, $\omega = 1.0$ |
| | 2 | | Nakagami | $m = 0.8$, $\omega = 1.0$ |
| | 3 | | Normal | $\mu = 0.9, \sigma = 0.4$ |
| | 4 | | Gamma | $a = 2.3$, $b = 0.4$ |

Table 22: Multipath fading distribution best fits for all measured use cases, in Room 2

| Use case | distance [m] | Rotation | Distribution | Parameters |
|---|---|---|---|---|
| U1 | 1 | 0° | Gamma | $a = 23.5$, $b = 0.1$ |
| | | 90° | Gamma | $a = 4.3$, $b = 0.2$ |
| | | 180° | Gamma | $a = 15.3$, $b = 0.1$ |
| | | 270° | Weibull | $a = 1.1$, $b = 7.7$ |
| | 2 | 0° | Gamma | $a = 13.4$, $b = 0.1$ |
| | | 90° | Rician | $s = 0.8$, $\sigma = 0.4$ |
| | | 180° | Weibull | $a = 1.1$, $b = 3.0$ |
| | | 270° | Logormal | $\mu = -0.1, \sigma = 0.2$ |
| | 3 | 0° | Normal | $\mu = 1.0, \sigma = 0.3$ |
| | | 90° | Nakagami | $m = 0.9$, $\omega = 1.0$ |
| | | 180° | Rician | $s = 0.6$, $\sigma = 0.6$ |
| | | 270° | Lognormal | $\mu = -0.0, \sigma = 0.2$ |
| | 4 | 0° | Nakagami | $m = 2.4$, $\omega = 1.0$ |
| | | 90° | Nakagami | $m = 0.9$, $\omega = 1.0$ |
| | | 180° | Rician | $s = 0.6$, $\sigma = 0.6$ |
| | | 270° | Nakagami | $m = 4.1$, $\omega = 1.0$ |
| U2 | 1 | 0° | Rician | $s = 0.8$, $\sigma = 0.5$ |
| | | 90° | Nakagami | $m = 1.1$, $\omega = 1.0$ |
| | | 180° | Weibull | $a = 1.1$, $b = 5.3$ |
| | | 270° | Weibull | $a = 1.0$, $b = 10.3$ |
| | 2 | 0° | Gamma | $a = 13.8$, $b = 0.1$ |
| | | 90° | Weibull | $a = 1.0$, $b = 1.9$ |
| | | 180° | Nakagami | $m = 1.8$, $\omega = 1.0$ |
| | | 270° | Normal | $\mu = 1.0, \sigma = 0.1$ |
| | 3 | 0° | Weibull | $a = 1.1$, $b = 2.9$ |
| | | 90° | Nakagami | $m = 1.2$, $\omega = 1.0$ |
| | | 180° | Nakagami | $m = 2.1$, $\omega = 1.0$ |
| | | 270° | Lognormal | $\mu = 0.0, \sigma = 0.2$ |
| | 4 | 0° | Nakagami | $m = 3.6$, $\omega = 1.0$ |
| | | 90° | Rician | $s = 0.6$, $\sigma = 0.5$ |
| | | 180° | Weibull | $a = 1.1$, $b = 3.1$ |
| | | 270° | Gamma | $a = 10.0$, $b = 0.1$ |
| U3 | 1-4 | 0° | Nakagami | $m = 4.0$, $\omega = 1.0$ |
| | | 180° | Rician | $s = 0.8$, $\sigma = 0.4$ |
| NB | 1 | 0° | Weibull | $a = 1.1$, $b = 7.7$ |
| | 2 | | Lognormal | $\mu = -0.1, \sigma = 0.3$ |
| | 3 | | Rician | $s = 0.9$, $\sigma = 0.3$ |
| | 4 | | Normal | $\mu = 1.0, \sigma = 0.3$ |

## A.4 Coherence bandwidth

Table 23: Coherence bandwidth for various use cases and conditions in different environments

| Use case | Environment | Rotation | $B_{coh[\mathrm{MHz}]}$ | | | | $B_{coh[\mathrm{MHz}]}$ (Gaussian) | | | |
|---|---|---|---|---|---|---|---|---|---|---|
| | | | 1m | 2m | 3m | 4m | 1m | 2m | 3m | 4m |
| U1 | Room 1 | 0° | 13 | 15 | 9 | 23 | 8 | 15 | 8 | 6 |
| | | 90° | 7 | 6 | 11 | 8 | 8 | 6 | 5 | 7 |
| | | 180° | 9 | 11 | 9 | 6 | 7 | 7 | 6 | 5 |
| | | 270° | 14 | 8 | 6 | 14 | 13 | 9 | 5 | 8 |
| | Room 2 | 0° | 7 | 10 | 7 | 6 | 7 | 5 | 6 | 6 |
| | | 90° | 7 | 4 | 6 | 6 | 4 | 4 | 4 | 5 |
| | | 180° | 6 | 8 | 5 | 5 | 5 | 7 | 5 | 5 |
| | | 270° | 35 | 8 | 7 | 7 | 8 | 6 | 6 | 6 |
| | Anechoic chamber | 0° | 30 | 16 | 43 | 18 | 16 | 18 | 19 | 19 |
| | | 90° | 1 | 1 | 1 | 1 | 1 | 1 | 1 | 1 |
| | | 180° | 6 | 7 | 1 | 1 | 1 | 1 | 1 | 1 |
| | | 270° | 21 | 18 | 17 | 13 | 14 | 16 | 1 | 1 |
| U2 | Room 1 | 0° | 11 | 13 | 12 | 11 | 9 | 12 | 6 | 6 |
| | | 90° | 7 | 7 | 9 | 13 | 5 | 7 | 7 | 7 |
| | | 180° | 9 | 8 | 8 | 13 | 8 | 6 | 6 | 8 |
| | | 270° | 13 | 14 | 15 | 20 | 9 | 13 | 10 | 11 |
| | Room 2 | 0° | 6 | 7 | 8 | 7 | 7 | 6 | 7 | 5 |
| | | 90° | 6 | 5 | 6 | 6 | 4 | 5 | 5 | 5 |
| | | 180° | 88 | 7 | 6 | 6 | 6 | 10 | 5 | 5 |
| | | 270° | 55 | 11 | 8 | 10 | 12 | 6 | 9 | 9 |
| | Anechoic chamber | 0° | 21 | 19 | 21 | 22 | 17 | 18 | 27 | 19 |
| | | 90° | 11 | 10 | 13 | 23 | 11 | 15 | 15 | 19 |
| | | 180° | 15 | 18 | 19 | 22 | 13 | 16 | 17 | 47 |
| | | 270° | 24 | 23 | 23 | 23 | 14 | 19 | 25 | 30 |
| U3 | Room 1 | 0° | 17 | | | | 12 | | | |
| | | 180° | 12 | | | | 9 | | | |
| | Room 2 | 0° | 40 | | | | 9 | | | |
| | | 180° | 17 | | | | 6 | | | |
| | Anechoic chamber | 0° | 108 | | | | 26 | | | |
| | | 180° | 35 | | | | 15 | | | |
| NB | Room 1 | 0° | 14 | 8 | 6 | 16 | 8 | 5 | 6 | 9 |
| | Room 2 | | 11 | 11 | 10 | 4 | 5 | 8 | 7 | 6 |
| | Anechoic chamber | | 22 | 28 | 20 | 16 | 13 | 12 | 12 | 7 |

## A.5 Delay spread

Table 24: RMS delay spread, $\sigma_\tau$[ns] in Anechoic chamber

| Use case | Rotation | $\sigma_\tau$[ns] | | | |
|---|---|---|---|---|---|
| | | 1 | 2 | 3 | 4 |
| U1 | 0° | 2.9 | 2.5 | 2.2 | 3.8 |
| | 90° | 9.6 | 5.0 | 6.2 | 4.6 |
| | 180° | 5.8 | 8.5 | 10.0 | 5.2 |
| | 270° | 2.2 | 2.3 | 2.9 | 2.6 |
| U2 | 0° | 2.6 | 2.8 | 2.6 | 2.9 |
| | 90° | 5.8 | 8.6 | 8.0 | 3.6 |
| | 180° | 4.2 | 4.3 | 3.9 | 3.2 |
| | 270° | 2.3 | 2.0 | 2.9 | 2.4 |
| U3 | 0° | 2.6 | | | |
| | 180° | 5.4 | | | |
| NB | 0° | 2.6 | 2.3 | 2.4 | 3.0 |

Table 25: RMS delay spread, $\sigma_\tau$[ns] in Room 1

| Use case | Rotation | $\sigma_\tau$[ns] | | | |
|---|---|---|---|---|---|
| | | 1m | 2m | 3m | 4m |
| U1 | 0° | 9.9 | 11.4 | 18.4 | 19.9 |
| | 90° | 23.1 | 17.5 | 18.5 | 21.4 |
| | 180° | 14.4 | 17.9 | 15.4 | 15.4 |
| | 270° | 8.7 | 15.4 | 19.4 | 13.0 |
| U2 | 0° | 15.9 | 19.8 | 19.0 | 20.1 |
| | 90° | 21.5 | 18.6 | 22.1 | 19.5 |
| | 180° | 17.8 | 18.0 | 19.5 | 19.7 |
| | 270° | 6.5 | 13.5 | 12.2 | 17.9 |
| U3 | 0° | 18.5 | | | |
| | 180° | 18.8 | | | |
| NB | 0° | 14.9 | 17.6 | 19.1 | 26.5 |

Table 26: RMS delay spread, $\sigma_\tau$[ns] in Room 2

| Use case | Rotation | $\sigma_\tau$[ns] | | | |
|---|---|---|---|---|---|
| | | 1 | 2 | 3 | 4 |
| U1 | 0° | 10.0 | 9.5 | 17.3 | 18.1 |
| | 90° | 20.4 | 22.5 | 21.7 | 27.3 |
| | 180° | 14.3 | 15.6 | 29.5 | 27.0 |
| | 270° | 4.4 | 9.4 | 10.8 | 13.0 |
| U2 | 0° | 10.9 | 14.4 | 17.1 | 15.1 |
| | 90° | 22.5 | 24.0 | 23.8 | 25.9 |
| | 180° | 8.4 | 16.4 | 19.0 | 22.0 |
| | 270° | 3.5 | 7.1 | 10.5 | 14.2 |
| U3 | 0° | 7.4 | | | |
| | 180° | 25.8 | | | |
| NB | 0° | 7.5 | 13.3 | 16.8 | 19.2 |

Table 27: Delay dispersion in U4 and U5

| Parameters | Use case | | | |
|---|---|---|---|---|
| | U4 | | U5 | |
| | 0° | 90° | 0° | 90° |
| RMS delay, $\sigma_\tau$[ns] | 20.4 | 18.6 | 7.3 | 12.7 |
| $B_{coh[\mathrm{MHz}]}$ | 6 | 7 | 11 | 9 |
| $B_{coh[\mathrm{MHz}]}$ (Gaussian) | 7 | 5 | 8 | 9 |

## A.6 Model validation

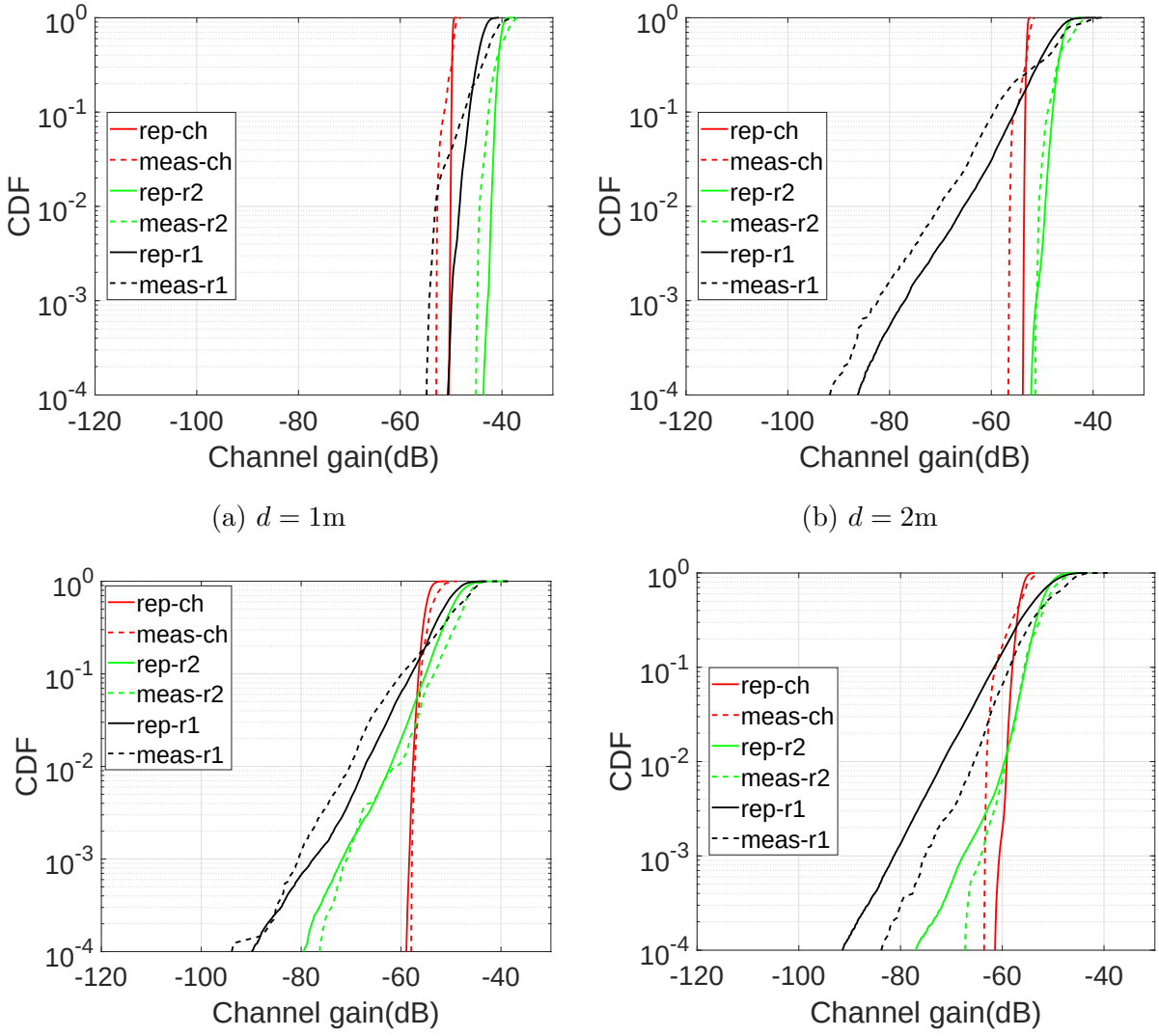


(a) $d = 1$m

(b) $d = 2$m

(c) $d = 3$m

(d) $d = 4$m

Figure 18: Comparison of the reproduced and measured channel gain for U1, 0° body orientation, at various Tx - Rx separation distances in Room 1, Room 2, and Anechoic chamber

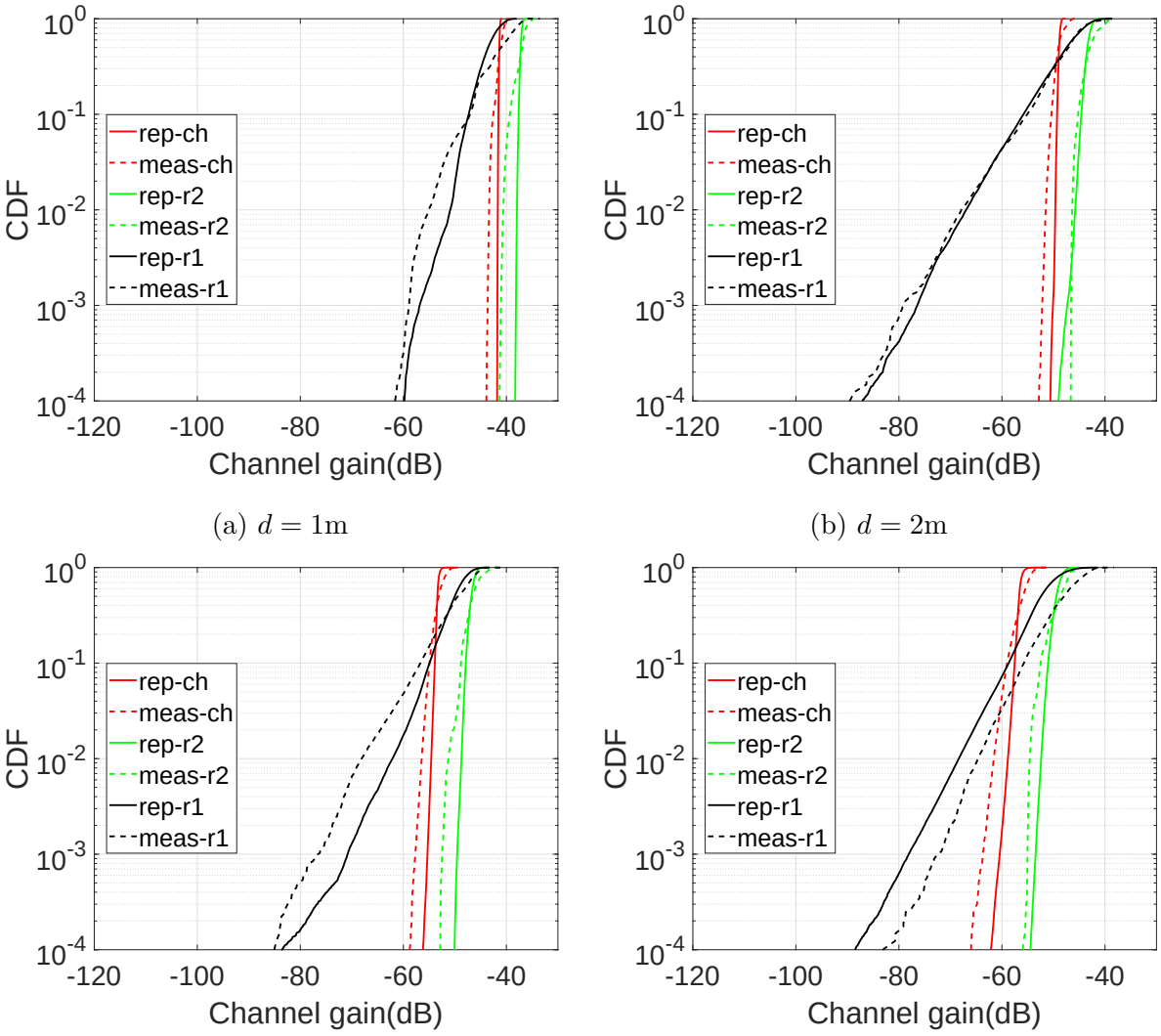


(a) $d = 1$m

(b) $d = 2$m

(c) $d = 3$m

(d) $d = 4$m

Figure 19: Comparison of the reproduced and measured channel gain for U1, 270° body orientation, at various Tx - Rx separation distances in Room 1, Room 2, and Anechoic chamber

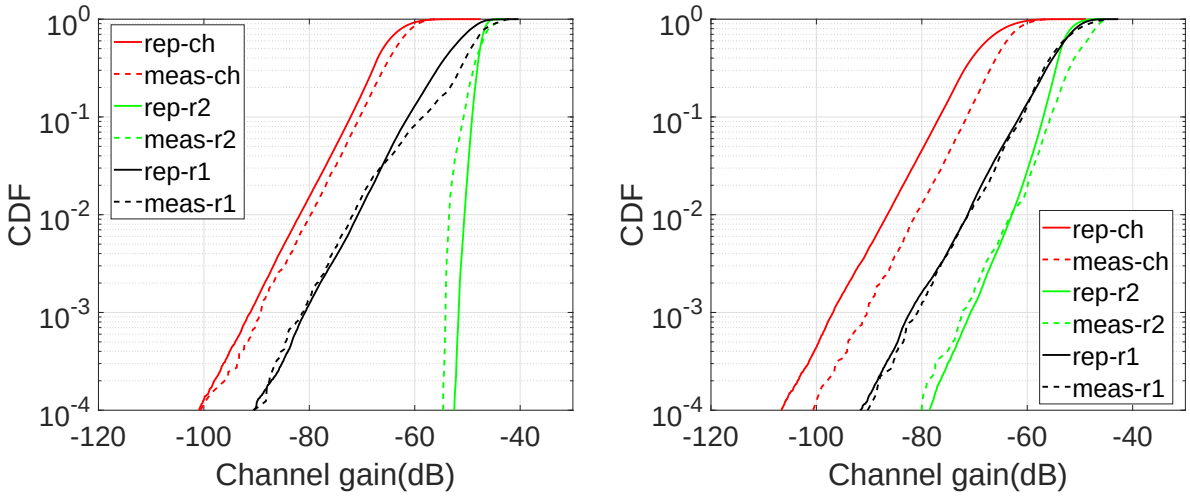


(a) $d = 1$m (b) $d = 2$m

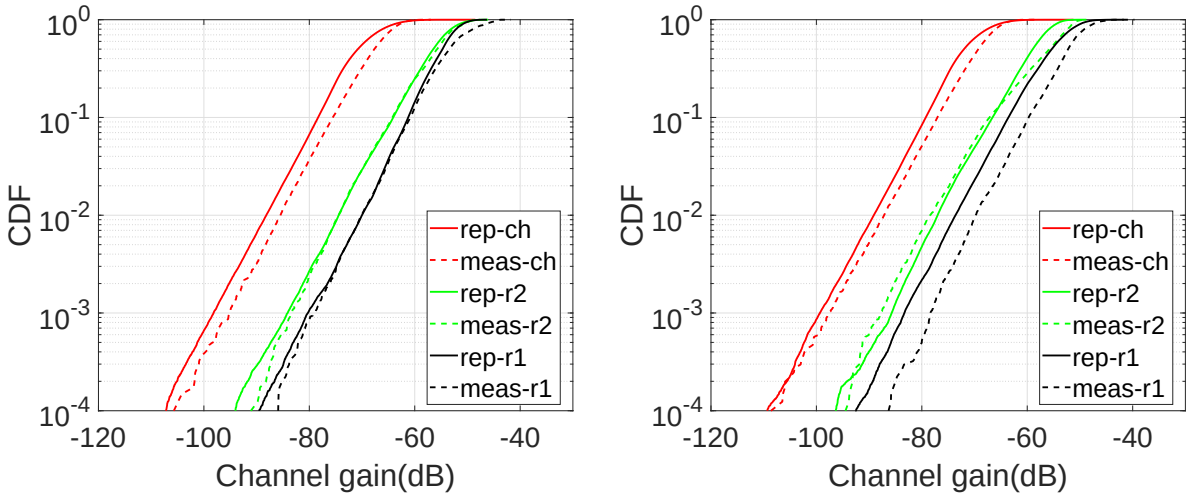


(c) $d = 3$m (d) $d = 4$m

Figure 20: Comparison of the reproduced and measured channel gain for U1, 180° body orientation, at various Tx - Rx separation distances in Room 1, Room 2, and Anechoic chamber

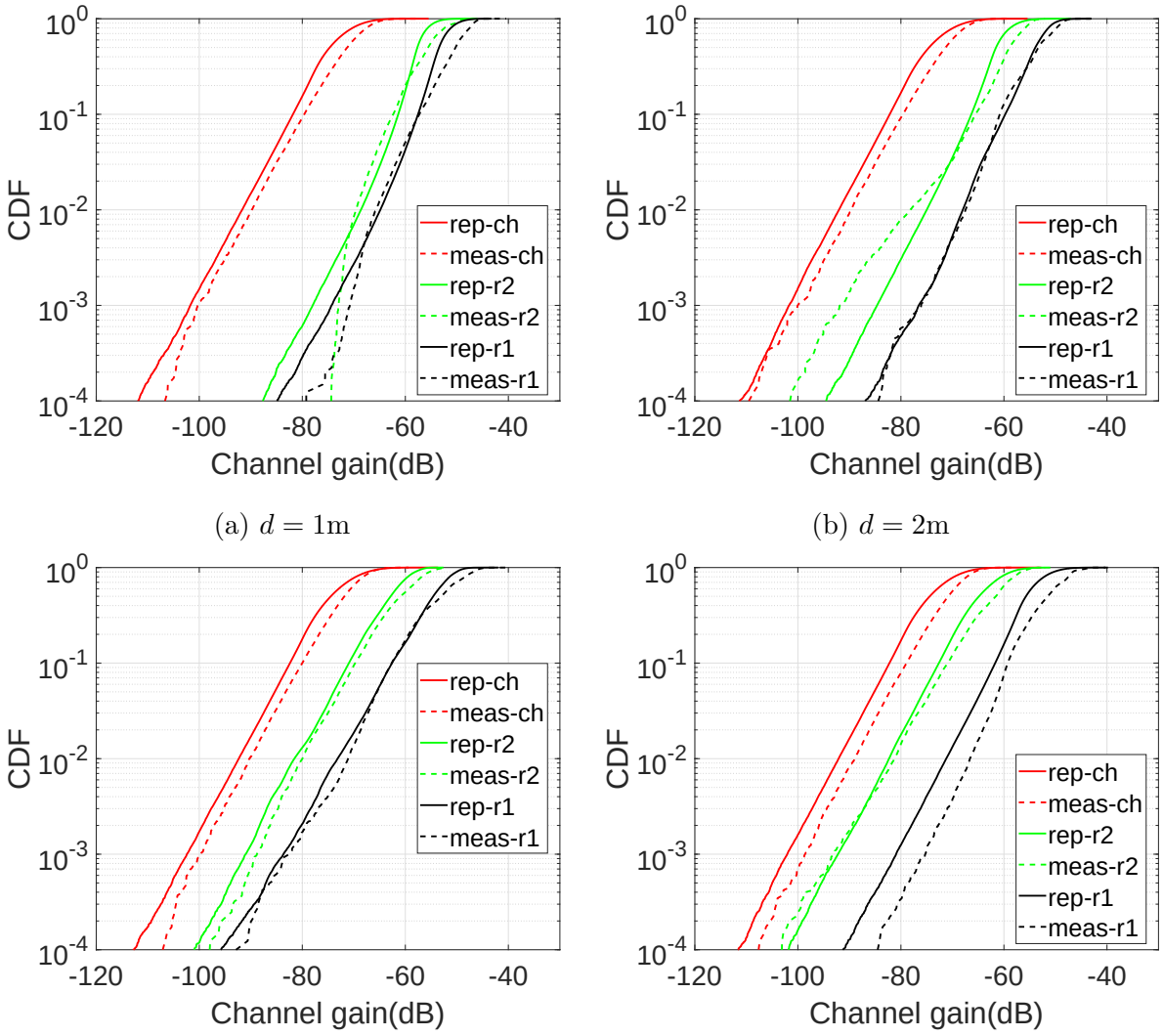


(a) $d = 1$m

(b) $d = 2$m

(c) $d = 3$m

(d) $d = 4$m

Figure 21: Comparison of the reproduced and measured channel gain for U1, 90° body orientation, at various Tx - Rx separation distances in Room 1, Room 2, and Anechoic chamber

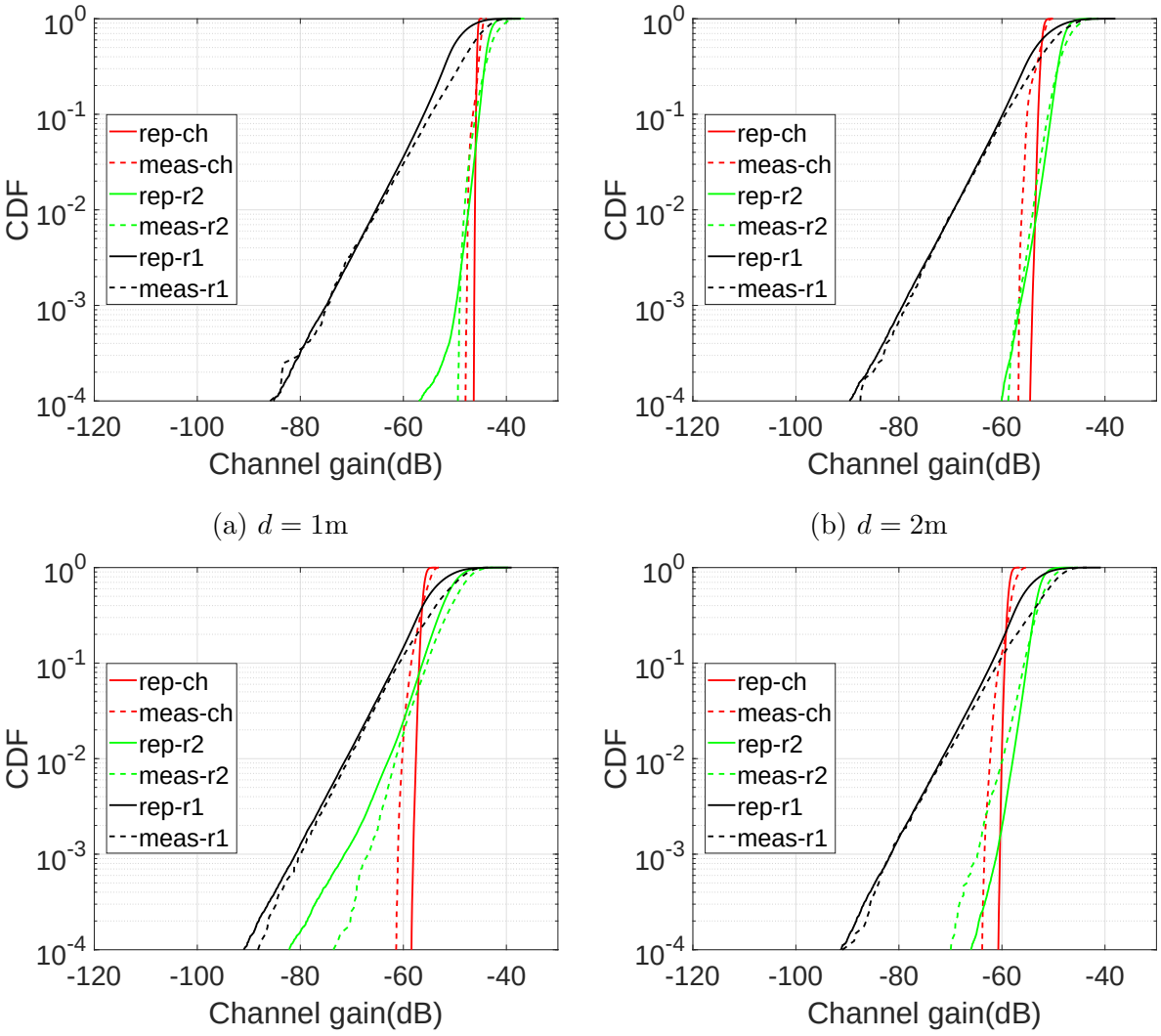


(a) $d = 1$m

(b) $d = 2$m

(c) $d = 3$m

(d) $d = 4$m

Figure 22: Comparison of the reproduced and measured channel gain for U2, 0° body orientation, at various Tx - Rx separation distances in Room 1, Room 2, and Anechoic chamber

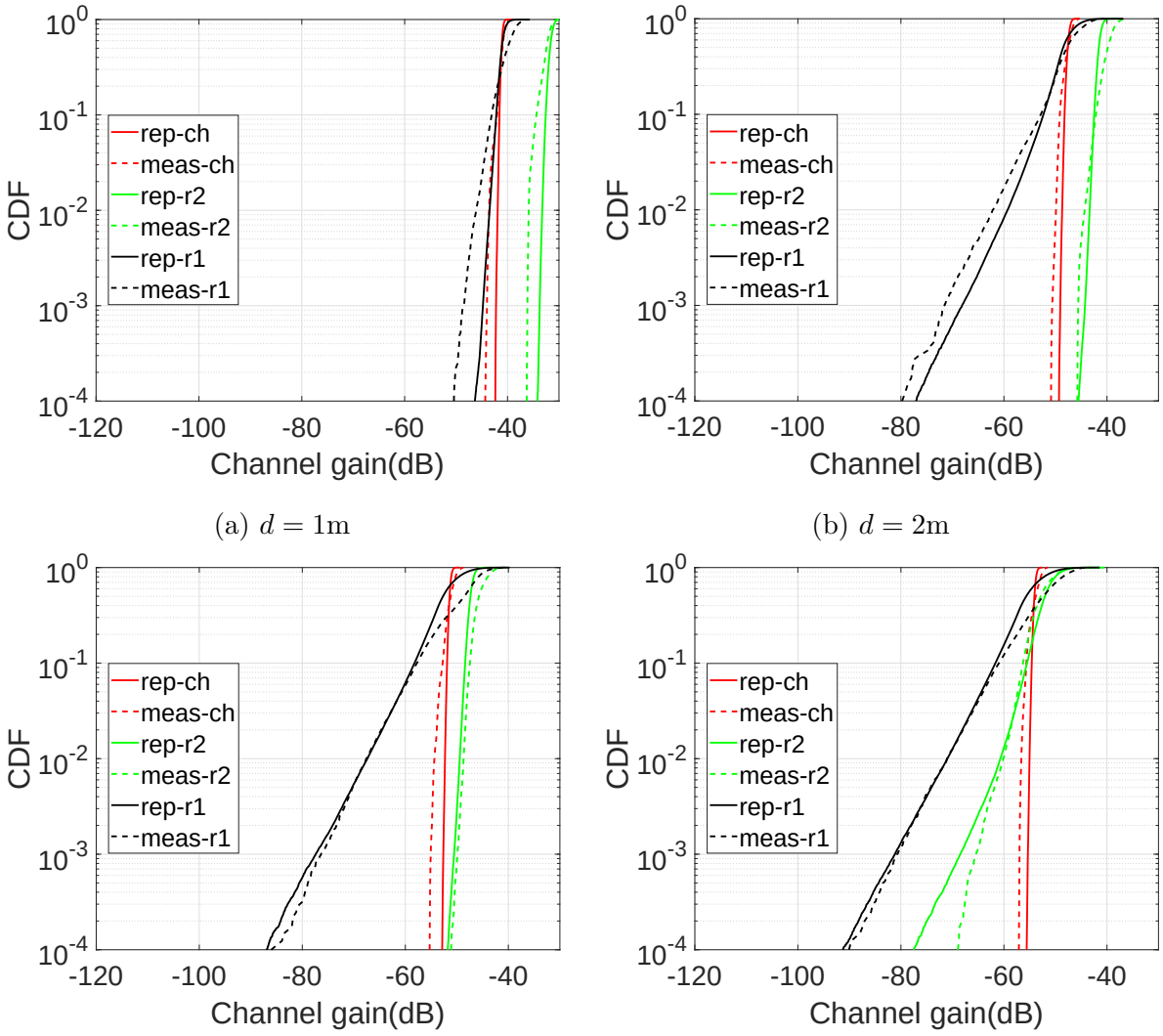


(a) $d = 1$m

(b) $d = 2$m

(c) $d = 3$m

(d) $d = 4$m

Figure 23: Comparison of the reproduced and measured channel gain for U2, 270° body orientation, at various Tx - Rx separation distances in Room 1, Room 2, and Anechoic chamber

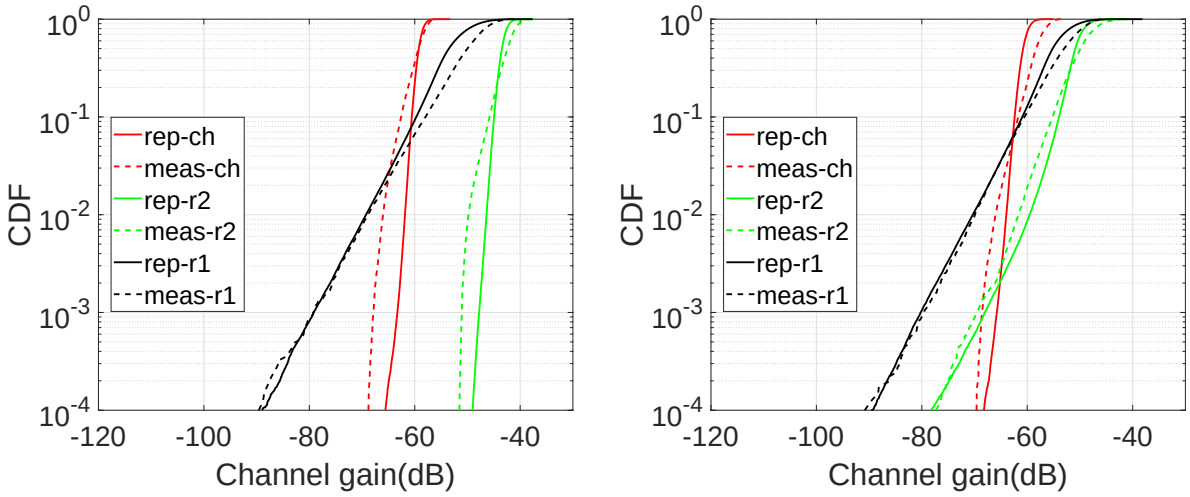


(a) $d = 1$m (b) $d = 2$m

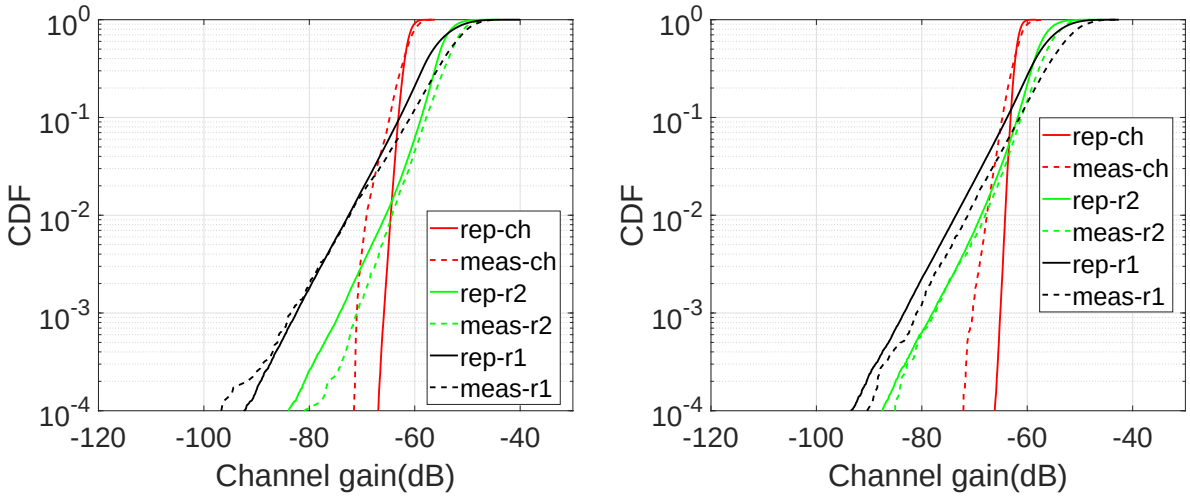


(c) $d = 3$m (d) $d = 4$m

Figure 24: Comparison of the reproduced and measured channel gain for U2, 180° body orientation, at various Tx - Rx separation distances in Room 1, Room 2, and Anechoic chamber

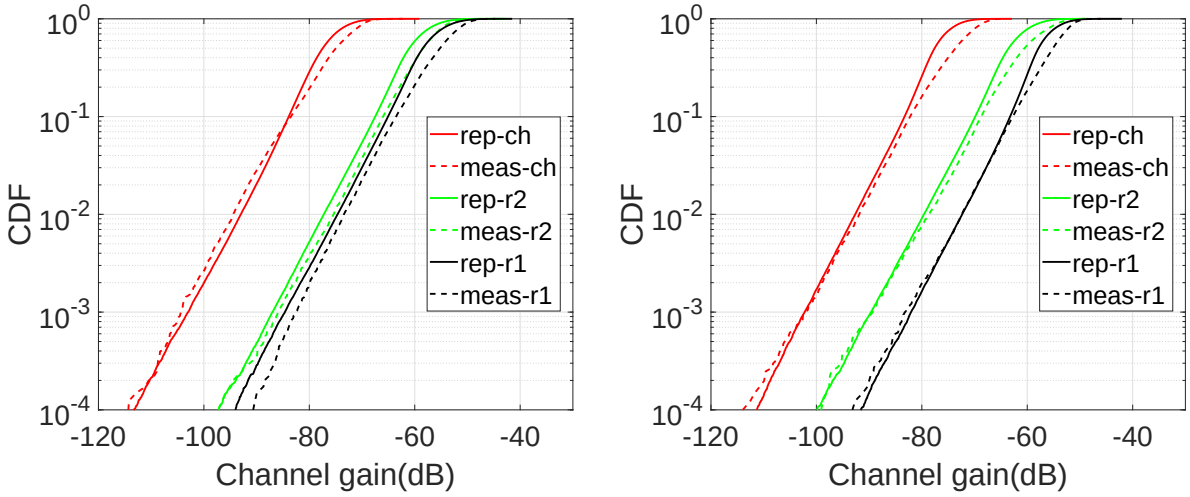


(a) $d = 1$m (b) $d = 2$m

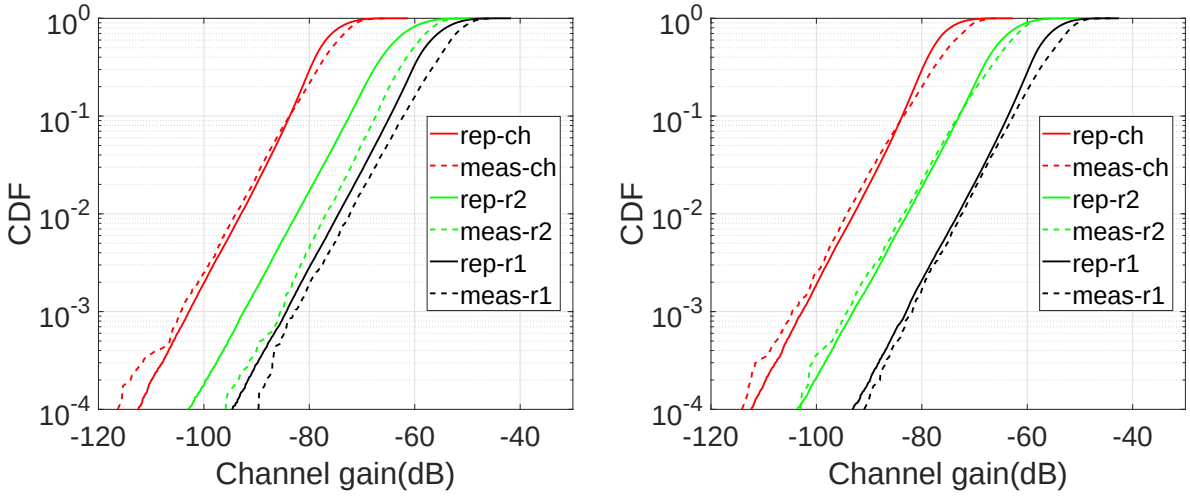


(c) $d = 3$m (d) $d = 4$m

Figure 25: Comparison of the reproduced and measured channel gain for U2, 90° body orientation, at various Tx - Rx separation distances in Room 1, Room 2, and Anechoic chamber